TITLE

Human Satellite 3 DNA encodes megabase-scale transcription factor binding platforms

AUTHORS

J. Matthew Franklin[1], Danilo Dubocanin[1], Cy Chittenden[1], Ashlie Barillas[1], Rosa Jooyoung Lee[1], Rajarshi P. Ghosh[2-3], Jennifer L. Gerton[4], Kun-Liang Guan[5,*], Nicolas Altemose[1,6,*]

AFFILIATIONS

1. Department of Genetics, Stanford University, Palo Alto, CA 94304, USA
2. Department of Molecular & Cell Biology, University of California, Berkeley, CA 94720, USA
3. Howard Hughes Medical Institute, University of California, Berkeley, CA 94720, USA
4. Stowers Institute for Medical Research, Kansas City, MO 64110, USA
5. Westlake University, School of Life Sciences, Hangzhou, Zhejiang, China
6. Chan Zuckerberg Biohub – San Francisco, San Francisco, CA 94158, USA

* Corresponding authors; altemose@stanford.edu, guankunliang@westlake.edu.cn

ABSTRACT

Eukaryotic genomes frequently contain large arrays of tandem repeats, called satellite DNA. While some satellite DNAs participate in centromere function, others do not. For example, Human Satellite 3 (HSat3) forms the largest satellite DNA arrays in the human genome, but these multi-megabase regions were almost fully excluded from genome assemblies until recently, and their potential functions remain understudied and largely unknown. To address this, we performed a systematic screen for HSat3 binding proteins. Our work revealed that HSat3 contains millions of copies of transcription factor (TF) motifs bound by over a dozen TFs from various signaling pathways, including the growth-regulating transcription effector family TEAD1-4 from the Hippo pathway. Imaging experiments show that TEAD recruits the co-activator YAP to HSat3 regions in a cell-state specific manner. Using synthetic reporter assays, targeted repression of HSat3, inducible degradation of YAP, and super-resolution microscopy, we show that HSat3 arrays can localize YAP/TEAD inside the nucleolus, enhancing RNA Polymerase I activity. Beyond discovering a direct relationship between the Hippo pathway and ribosomal DNA regulation, this work demonstrates that satellite DNA can encode multiple transcription factor binding motifs, defining an important functional role for these enormous genomic elements.

INTRODUCTION

Eukaryotic genomes often contain massive arrays of rapidly evolving repetitive DNA sequences called satellite DNA. The repeat units can range from a few bases to kilobases, and array lengths reach up to tens of megabases[1]. Although satellite DNAs were among the first sequences to be biochemically isolated and characterized in the early days of molecular biology, modern genomics research has largely excluded them[1], and our understanding of the origins and evolutionary mechanisms that maintain these megabase-scale structures remains incomplete.

Despite the general notion that satellite DNAs are transcriptionally silent and constitutively heterochromatic, examples of transcription factors (TFs) binding satellite DNA through motif recognition have been reported for mouse cells (Pax/9, Foxd3, YY11[2]), human cells (HSF1[3], DUX4[4], Ikaros[5], EWS-FLI1[6]), and *Drosophila*[7]. The biological functions of these interactions appear disparate, suggesting that the sequence content, chromatin composition, and genomic localization of satellite DNAs dictate the functional roles of these massive repetitive elements.

Recent efforts using long-read sequencing have established complete “Telomere-to-Telomere” (T2T) assemblies of humans[8] and non-human primates[9]. These T2T assemblies provide unprecedented characterizations of satellite DNAs in terms of sequence content and variation between individuals. In humans, satellite DNAs are predominantly found at centromeres, peri-centromeres, the short arms of the acrocentric chromosomes (13-15, 21-22), and the long arm of chromosome Y. In total, this accounts for over 200 megabases, approximately 7% of the human genome[10].

To date, satellite DNA studies in humans traditionally focused on alpha satellite (αSat), the most abundant satellite DNA family, which provides an essential scaffold for assembly of the centromere and kinetochore on each chromosome. Recently, a search for αSat binding transcription factors revealed multiple new interactions, including BRD4, which normally functions at enhancer elements[11]. The other major human satellite DNA families (Human Satellites 1, 2, 3, beta, gamma) have poorly understood biological functions, and their heterogeneous localization across chromosomes suggests they are not essential for centromere function.

Human Satellite 3 (HSat3) is the most abundant non-centromeric satellite in the human genome, representing approximately 2% of the genome. This family is defined by enrichment of GGAAT pentamers and is thought to have expanded along the great ape lineage[1]. The largest contiguous repetitive element in the human genome is an HSat3 array adjacent to the chromosome 9 centromere, spanning 28 megabases[10]. Notably,

the acrocentric chromosomes (13-15, 21, 22) contain large arrays of ribosomal RNA genes (rDNAs) that are bookended by all the major satellite DNA repeat families[10], including dozens of distinct HSat3 arrays ranging from ~1 kilobase to 8 megabases (Supplementary Figure 1). HSat3 DNA is generally thought to be packaged as constitutive heterochromatin, marked by high levels of methyl-CpG and H3K9me3-containing nucleosomes, and maintained in a silenced, compacted state[12]. However, a handful of reports describe enrichment of transcription factors (TFs) on HSat3[3,6,13,14].

Here, we report the results of a systematic search for HSat3-binding TFs using motif enrichment analysis and published ChIP-seq data. This effort revealed a set of HSat3-binding TFs from multiple, broadly important cell signaling pathways. We conducted functional studies of the top hit, TEAD, a highly conserved TF family from the Hippo pathway that plays vital roles in early development, organ size regulation, and cancer[15,16]. Based on evidence from super-resolution microscopy, RNA Polymerase I reporter assays, and genetic perturbations, we propose that HSat3-bound TEAD and its effectors regulate rDNA transcription in the nucleolus.

RESULTS

A transcription factor screen reveals candidate HSat3 binding factors

To systematically identify novel HSat3-binding transcription factors, we first scanned HSat3 arrays for known transcription factor motifs from the JASPAR database (828 vertebrate motifs)[17]. Annotated HSat3 sequences were sourced from the human T2T assembly T2T-CHM13v2.0[1] (Figure 1a). Although closely related, distinct HSat3 arrays within humans show sequence divergence. Using k-mer based clustering, HSat3 repeats can be split into two main subfamilies, HSat3A and HSat3B, each containing further subfamilies (HSat3A1-6, HSat3B1-5)[18]. We computed the enrichment of each known TF on each distinct HSat3 array, relative to the motif's frequency in gene promoters (Figure 1b). As expected, most known TF binding motifs are not enriched, given the highly constrained sequence space of repeat elements (Figure 1c, Supplementary data). However, we found that 42 TF motifs are enriched at least 10-fold compared to background, sometimes with HSat3 subfamily-specific enrichment profiles (Figure 1c).

Across all HSat3 arrays, the TEAD and NFAT TF families represent the most highly enriched motifs, followed by SOX1, LIN54, IRF3, MYB, OVOL1, DUX4, and NKX2-4 (Figure 1d). Previously described as an HSat2 binding factor, the DUX4 motif is also highly enriched in HSat3. Both HSat2 and HSat3 are enriched for GGAAT pentamers, but HSat2 has a longer, variable repeat unit which has diverged from HSat3[19]. Although previously validated[20], HSF1 is ranked 15th in terms of motif enrichment. Although the top enriched motifs are generally consistent among HSat3 subfamilies (Figure 1e, Supplementary Figure 2), the Y-chromosome specific subfamily HSat3A6 contained unique motif enrichments for bcl11B, CDX4, ETV5-FOX01, and HOXD9 (Figure 1e). This is consistent with the strong sequence divergence of HSat3A6[1]. Surprisingly, ETV5-FOX01 is the only ETS-family motif heavily enriched in HSat3, despite the core GGAA-motif found in most ETS consensus motifs[17] (Supplementary Figure 3).

Notably, the well-characterized TEAD DNA binding motifs contain a constrained core GGAATG, which is recapitulated by tandemly repeated GGAAT HSat3 pentamers (Figure 1f). Similarly, NFAT-family motifs consistently contain GGAA in the consensus motif (Figure 1f). We estimated that the percentage of total TEAD motifs across the human genome in HSat3 ranges from 24-58% using ChIP-seq derived motifs in JASPAR (Supplementary Figure 4). However, all TEAD-family factors contain a highly constrained GGAATG 6 base pair core. Approximately 72% of genome-wide matches to these core motifs occur in HSat3 (Supplementary Figure 4).

Figure 1:

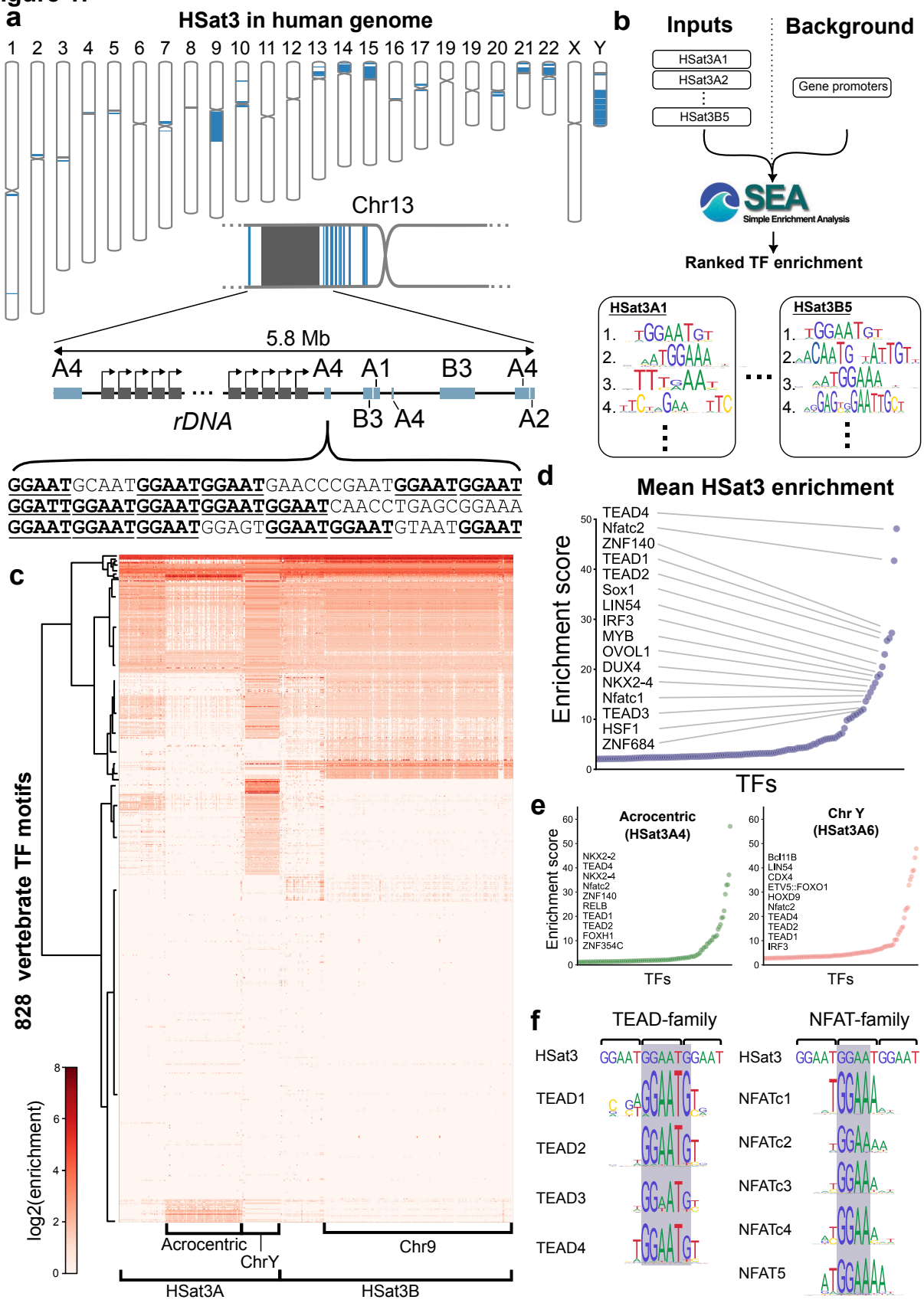
a
HSat3 in human genome
1 2 3 4 5 6 7 8 9 10 11 12 13 14 15 16 17 19 19 20 21 22 X Y
Chr13
5.8 Mb
A4 A4 A1 B3 A4
rDNA
B3 A4 A2
GGAATGCAATGGAATGGAATGAACCCGAATGGAATGGAAT
GGATTGGAATGGAATGGAATGGAATCAACCTGAGCGGAAA
GGAATGGAATGGAATGGAGTGGAATGGAATGTAATGGAAT
b
Inputs
Background
HSat3A1
HSat3A2
HSat3B5
Gene promoters
SEA
Simple Enrichment Analysis
Ranked TF enrichment
HSat3A1
HSat3B5
c
828 vertebrate TF motifs
log2(enrichment)
Acrocentric
ChrY
Chr9
HSat3A
HSat3B
d
Mean HSat3 enrichment
Enrichment score
TEAD4
Nfatc2
ZNF140
TEAD1
TEAD2
Sox1
LIN54
IRF3
MYB
OVOL1
DUX4
NKX2-4
Nfatc1
TEAD3
HSF1
ZNF684
TFs
e
Acrocentric (HSat3A4)
NKX2-2
TEAD4
NKX2-4
Nfatc2
ZNF140
RELB
TEAD1
TEAD2
FOXH1
ZNF354C
Chr Y (HSat3A6)
Bcl11B
LIN54
CDX4
ETV5::FOXO1
HOXD9
Nfatc2
TEAD4
TEAD2
TEAD1
IRF3
f
TEAD-family
NFAT-family
HSat3
TEAD1
TEAD2
TEAD3
TEAD4
NFATc1
NFATc2
NFATc3
NFATc4
NFAT5

Figure 1: A search for transcription factor motifs enriched in HSat3. (a) Top: karyogram of the human genome with HSat3 arrays marked in blue. Note the large arrays on chromosomes 9, 15, Y. Middle: Depiction of HSat3 (blue) and rDNA (grey) organization on chromosome 13 p-arm. Individual HSat3 arrays are annotated with subfamily names. Bottom: sample of HSat3A4 DNA sequence with GGAAT pentamers in bold with underline. (b) Flow diagram of the motif enrichment search using SEA from MEME-Suite. (c) Heat-map of predicted TF motifs enriched on each HSat3 array instance in the chm13v2.0 genome. Columns are individual HSat3 arrays, rows are individual TF motifs organized by hierarchical clustering. (d) Mean enrichment scores for each TF across all HSat3 arrays, with labels for the top 16 TFs. (e) HSat3 sub-family specific enrichment scores with top 10 motifs labeled for the acrocentric-specific subfamily HSat3A4 and the chromosome Y-specific subfamily HSat3A6. (f) Correspondence between the HSat3 pentamer repeat and the TEAD- and NFAT-family consensus motifs (logo diagrams from JASPAR[17]).

As many of these candidate factors are not known to bind HSat3, we turned to existing ChIP-seq data to corroborate our predictions. Standard ChIP-seq pipelines mask out repetitive regions, possibly explaining the dearth of established HSat3 factors despite the strong enrichment of TF motifs. The ENCODE database has standardized high-quality ChIP-seq datasets across many cell types and factors[21]. To utilize this rich dataset we re-mapped the data to theT2T-CHM13v2.0 assembly[22]. A similar approach was previously taken to identify factors that bind αSat[11].

We defined the enrichment score as the coverage ratio of HSat3 arrays to random control regions for the ChIP pull-down and the input DNA (Figure 2a, Methods, Supplementary Data). This controls for specificity in both the ChIP pull-down and the input DNA. Mapping short-read sequencing data to repetitive DNA is inherently limited due to multiple mapping sites. To examine our ability to map short reads within HSat3 arrays, we used existing Heat-shock Factor 1 (HSF1) ChIP-seq data from heat-shocked MCF7 cells[23]. HSF1 is well described as an HSat3-binding TF under cellular stress conditions, most notably following heat-shock[3]. Interestingly, HSF1 motifs were enriched in sub-regions of HSat3 arrays, in contrast to TEAD motifs, which are evenly distributed (Figure 2b). The HSF1 ChIP-seq data showed clear enrichment at HSat3 regions of high motif density. This example shows that short-read sequencing data can map broadly to predicted regions even within simple repeat arrays.

The enrichment scores for 1,067 targets across 13 commonly used cell lines revealed dozens of highly enriched factors (Figure 2c-d, supplementary data). The top 10 factors are mostly cell-line specific (Supplementary Figure 5), possibly reflecting cell-type specific functionality and TF expression.

Across cell lines, the only target showing HSat3 enrichment in both ChIP-seq and motif analysis was TEAD4 in HCT116 (Figure 2e, Supplementary Figure 6). This highlights the complementarity of the two approaches and some of the limitations of screens

175 **Figure 2:**

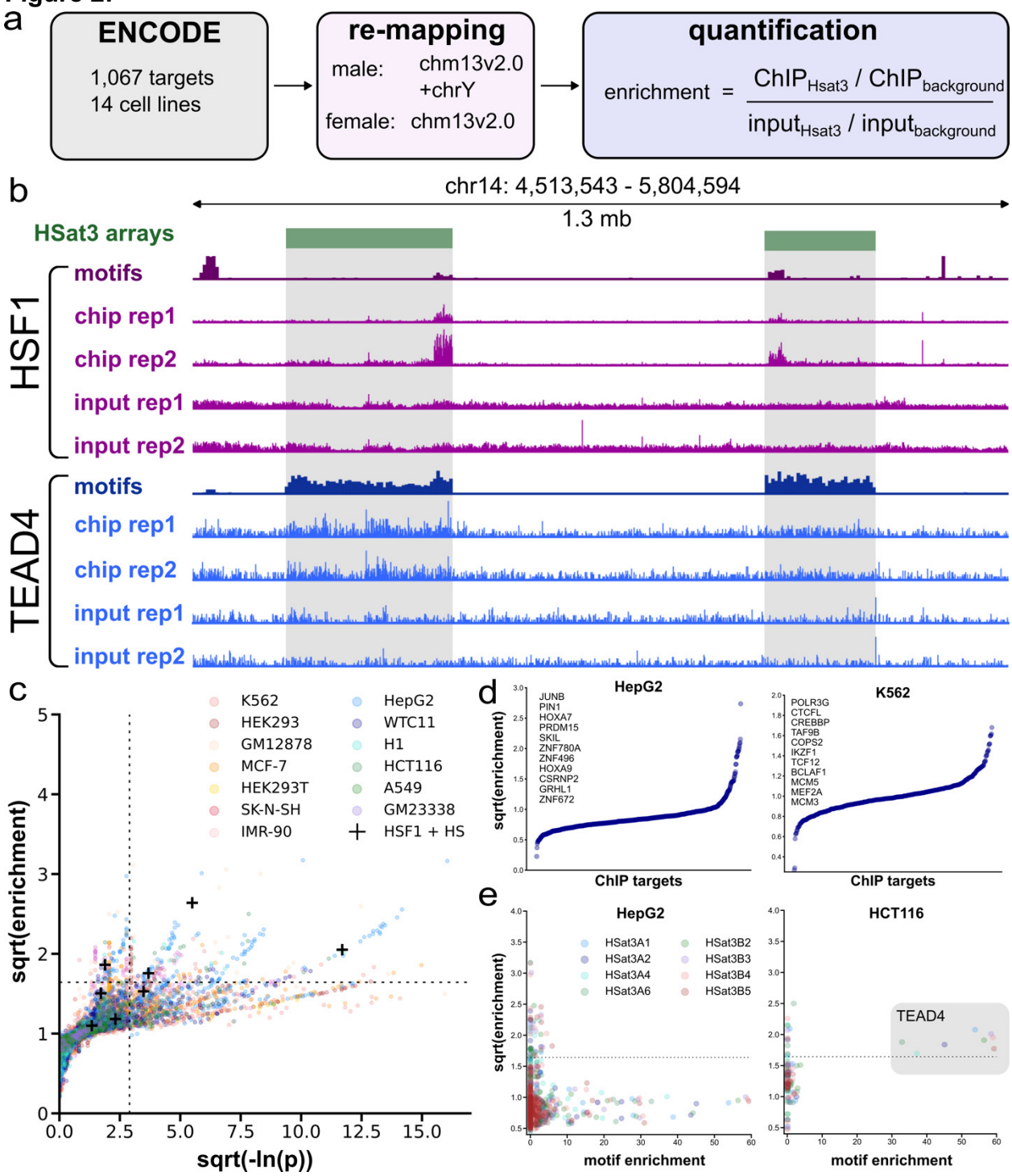

176

177 **Figure 2: ENCODE ChIP-seq database search for HSat3-binding factors.** (a) Flow diagram of ChIP-
178 seq analysis pipeline. Data were accessed directly from ENCODE. 1,067 ChIP-targets across 13 human
179 cell lines were mapped to the T2T-CHM13v2.0 assembly with or without chromosome Y depending on
180 cell line karyotype. Enrichment on HSat3 was calculated using the ratio of HSat3 to background for the
181 ChIP relative to the input DNA. (b) Demonstration of ChIP-seq reads enriched at TF motifs in HSat3.
182 HSF1 motifs are found in sub-regions of the HSat3 arrays (green blocks). HSF1 ChIP-seq reads in heat-

shocked MCF7 cells show specific enrichment in regions of high HSF1 motif density. TEAD4 motifs are enriched evenly across HSat3 arrays, and TEAD4 ChIP-seq in HTC116 cells shows read enrichment uniformly across HSat3. (c) Scatterplot of enrichment vs -ln(P) for the ChIP-seq screen. Data points are colored by cell line with markers for each HSat3 subfamily. ChIP-seq for HSF1 after heat-shock in MCF7 cells is highlighted with "+" markers as a positive control. (d) Ranked HSat3 enrichment scores for HepG2 (668 targets) and K562 (468 targets). (e) Correlation between ChIP-seq and motif enrichment for HepG2 (N=266 factors) and HCT116 (N=21 factors), colored by HSat3 subfamily. Data are plotted for subfamilies with more than 10 instances in the reference genome.

---

based on ChIP-seq enrichment in aggregate. For example, NFAT family members, which were highly enriched in the motif enrichment screen, were not found among the top TF candidates for any cell lines in our ChIP-seq screen. While TEADs are broadly expressed in most cell lines and constitutively nuclear, NFAT factors are only translocated into the nucleus following intracellular calcium activation via calcineurin[24]. The NFAT ENCODE datasets were not carried out in calcium activating conditions, thus potentially explaining the lack of HSat3 signal. We next sought to validate the top HSat3 candidates from both the motif and ChIP-seq analyses.

Imaging and sequencing validate TFs bound to HSat3

Immunostaining for HSF1 after heat shock shows distinct sub-nuclear foci due to the high density of binding sites on large HSat3 arrays[3]. Similarly, live imaging of dCas9 targeted to the chromosome 9 HSat3 array shows clear foci[25]. Thus, we reasoned that we could leverage the ability to image HSat3-associated foci to test our binding predictions. To that end, we cloned a library of the top candidate TFs tagged with mScarlet for transfection and live-cell imaging in 293T cells. Further, we generated a synthetic zinc-finger (ZF) array targeting 18 bp of the repeated HSat3 pentamer GGAAT to provide a colocalization fiducial, referred to as ZFsat3. ZFsat3-mScarlet shows punctate foci in live cells, and two-color immuno-FISH with pre-labeled anti-RFP-CF488A antibody and fluorophore-labeled HSat3 oligos showed a one-to-one colocalization, demonstrating highly specific HSat3 binding (Supplementary Figure 7).

Each mScarlet-tagged candidate TF was transiently transfected with ZFsat3-meGFP to assess HSat3 localization using live-cell microscopy (Figure 3a). As a positive control, we show previously identified HSat3 factors JRK and TIGD3 both co-localize with HSat3 foci (Supplementary Figure 8). TEAD1-mScarlet showed a one-to-one correspondence to ZFsat3 (Figure 3b), consistent with the near-perfect recapitulation of the TEAD consensus motif by HSat3 pentamers (Figure 1f). Similarly, TEAD1-4 tagged with meGFP showed similarly strong colocalization with ZFsat3-mScarlet (Supplementary Figure 8). TEAD-bound sites frequently contain multiple TEAD motifs in human enhancers[26], with the most common configuration being two motifs separated by 3 base pairs. Cooperative TEAD binding is suggested to occur at such repeated motifs, thus accumulation of TEADs at HSat3 may be driven by cooperativity.

225 NFAT factors are cytoplasmically localized until activation by intracellular calcium
226 release[24]. Following 1 hr treatment with 1 μM ionomycin, mScarlet-tagged NFATc1-3
227 and NFAT5 showed nuclear translocation in cells to HSat3 foci (Figure 3b,
228 Supplementary Figure 9a). In the Protein Atlas database, NFATc1 and NFATc4 both
229 show clear nuclear bodies[27]. Although NFAT localization to such bodies has long been
230 observed in fixed and live cell images[28], our data provide an underlying molecular
231 explanation.
232
233 Following activation of the core innate immunity response pathway, IRF3 is translocated
234 into the nucleus to drive interferon expression[29]. Live imaging of mScarlet-IRF3 showed
235 cytoplasmic localization in interphase 293T cells (Supplementary Figure 9b). However,
236 mitotic cells showed strong IRF3 enrichment at HSat3 foci (Figure 3b). Sub-nuclear
237 IRF3 foci have previously been identified and attributed to liquid-liquid phase separation
238 with interferon (IFN)-stimulated response element DNA[30]. Upon inspection, the
239 previously observed IRF3 foci resemble HSat3 foci, with tens of nuclear foci of variable
240 size. Our results suggest that HSat3 provides a scaffold of dense binding motifs that
241 drive this observed formation of nuclear foci.
242
243 The other evaluated top candidates SOX1 and NKX2-2 did not show overt localization
244 to all ZFsat3-foci, however both SOX1 and NKX2-2 showed colocalization to a small
245 subset of ZFsat3 foci (Supplementary Figure 10). Surprisingly, the CUT homeo-domain
246 factor CUX1 showed strong colocalization with ZFsat3 (Figure 3b), despite being ranked
247 31st for mean HSat3 binding in the motif-enrichment screen. The other CUT family
248 members CUX2, ONECUT1, ONECUT2 have similar DNA binding domains and motifs,
249 suggesting this family is likely to bind HSat3 (Supplementary Figure 11). Although the
250 ZFsat3-megfp may be competing with HSat3-binding TFs, our results highlight that
251 simple motif enrichment predicts the binding of many satellite DNA TFs.
252
253 Because the ChIP-seq screen revealed tens of candidate factors per cell line, we
254 filtered our predictions using microscopy images showing protein localization to nuclear
255 bodies or foci from Protein Atlas[27] and existing literature. Ranked 4th in HepG2
256 (enrichment ratio=4.34), published PRDM15 immunofluorescence images show striking
257 localization to nuclear bodies[27,31]. In our colocalization assay, PRDM15 showed strong
258 colocalization to HSat3 (Figure 3b). The JASPAR PRDM15 motif does not enrich in
259 HSat3 (rank= 751/868). However, a reported consensus motif from mouse ChIP-seq
260 data shows highly constrained AA and GG dinucleotides separated by 5 bases[32].
261 Flexibility in the ZF array may allow PRDM15 to bind AA and GG dinucleotides
262 separated by 6 bases, which is found in to end-to-end HSat3 pentamers. We
263 hypothesized that HSat3 localization may be mediated through the ZF array present on
264 the C-terminus of PRDM family factors[33]. Truncated PRDM15 containing only the ZF

Figure 3:

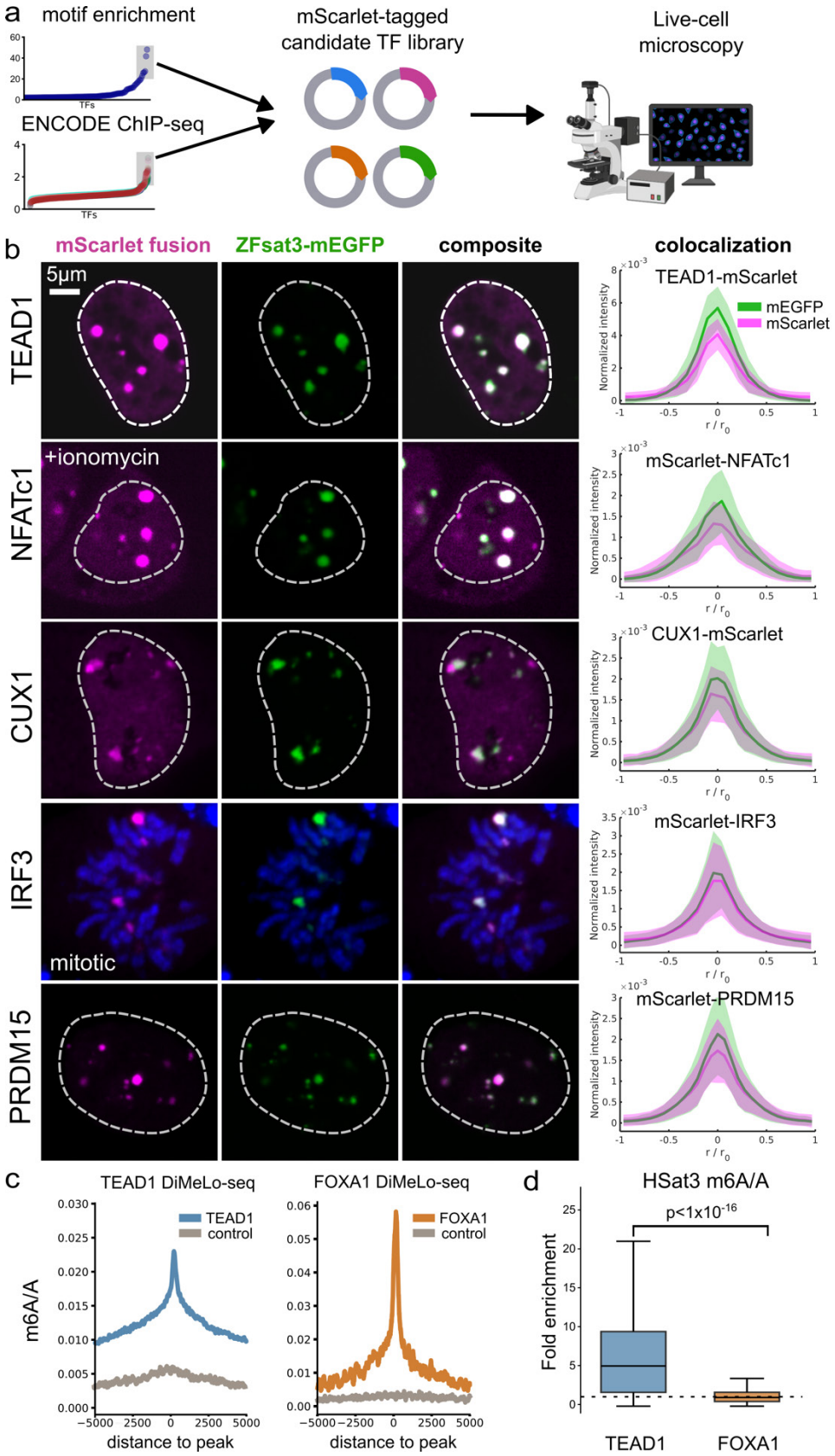
a
motif enrichment
ENCODE ChIP-seq
TFs
mScarlet-tagged candidate TF library
Live-cell microscopy
b
mScarlet fusion
ZFsat3-mEGFP
composite
colocalization
5µm
TEAD1
NFATc1
+ionomycin
CUX1
IRF3
mitotic
PRDM15
TEAD1-mScarlet
mEGFP
mScarlet
mScarlet-NFATc1
CUX1-mScarlet
mScarlet-IRF3
mScarlet-PRDM15
Normalized intensity
r / r0
c
TEAD1 DiMeLo-seq
FOXA1 DiMeLo-seq
TEAD1
control
FOXA1
control
m6A/A
distance to peak
d
HSat3 m6A/A
p<1x10-16
Fold enrichment
TEAD1
FOXA1

Figure 3: Validation of predicted HSat3-binding factors. (a) Flow diagram of the validation pipeline. Top candidate factors from both motif searches and ChIP-seq analysis were tagged with mScarlet in a pHIV EF1α lentivirus expression vector. Transfected candidate TFs were evaluated with live-cell microscopy. (b) Representative confocal images of TF-mScarlet and ZFsat3-mEGFP co-transfected in 293T cells for validated HSat3 factors TEAD1, NFATc1, CUX1, IRF3, and PRDM15. All images are single z-planes. Due to the high binding capacity for HSat3, foci intensities are extremely bright compared to nucleoplasm, thus outlines of cell nuclei are shown by dashed lines. Right panels show intensity profile analysis of 3D segmented HSat3 foci with normalized intensity and the spatial dimension. The number of foci used for each distribution are as follows: N(TEAD1)=10, N(NFATc1)=20, N(CUX1)=15, N(IRF3)=12, N(PRDM15)=15. The solid line represents the mean and the shaded regions represent the standard deviation. (c) Results of DiMeLo-seq for TEAD1-mScarlet (HSat3 binding), FOXA1-mScarlet (non-HSat3 targeting), and wildtype 293Ts not expressing mScarlet. The fraction of m6A-modified bases (m6A/A) was calculated for reads centered at the respective ChIP-seq peaks for TEAD1 and FOXA1 in non-repetitive regions. (d) Enrichment of m6A/A across all HSat3-aligned DiMeLo-seq reads for either TEAD1 and FOXA1, relative to control cells. The box plot lines are as follows: center line, median; box limits, upper and lower quartiles; whiskers, 1.5x interquartile range. A one-tailed Wilcoxon rank sum test was performed to compare m6A/A enrichment in HSat3 between TEAD1 and FOXA1.

array localized to HSat3, further suggesting direct binding via DNA motif recognition, although ZF-protein interactions cannot be ruled out (Supplementary Figure 12). Such flexible binding modes are reported for ZNF512 and ZNF512B, which have longer linkers between ZFs, aiding their ability to recognize repetitive DNA between species[34].

Other tested ChIP-seq candidates JUNB, HOXA9, HOXA7, and HOXA9 did not show HSat3 co-localization in 293T transient transfection (Supplementary Figure 13). In the future, expanding the screen to test the ChIP-seq hits using the respective cell lines in which the factors showed HSat3 enrichment will be needed to thoroughly capture all HSat3-binding factors. Given the strong HSat3 colocalization in our imaging screen, the lack of NFAT and TEAD enrichment in ChIP-seq could be due to variations between cell lines, antibodies, and sample preparations.

We further validated TEAD binding to HSat3 using DiMeLo-seq. This technique maps protein-DNA interactions by recruiting an adenine DNA methyltransferase to a target protein, depositing exogenous methyl-6-adenine (m6A) marks, and reading the modified bases using long-read sequencing[35]. This allows accurate mapping of reads to repetitive regions of the genome. Anti-mScarlet DiMeLo-seq on TEAD1-mScarlet expressing 293T cells showed clear enrichment at known TEAD ChIP-seq peaks (Figure 3c), and a 6.25-fold increase in HSat3 methylation compared to control cells, whereas the non-HSat3 enriched TF FOXA1 showed only a 1.59-fold increase in HSat3 methylation (Figure 3d).

Our data show that repetitive DNA can act as an endogenous recruitment platform for many TFs, explaining previous observations of nuclear-body localized PRMD15 and

310 NFAT-family factors. However, our catalog of HSat3-binding factors is not exhaustive.
311 The motif enrichment strategy employed is relatively simple, and would not account for
312 non-linear effects like binding cooperativity due to proximity of multiple weak sites.
313 Further, these identified interactions imply that ChIP-seq derived motifs may be biased
314 in predicting the true consensus sequence due to ignoring binding sites in repetitive
315 regions.
316
317 Utilizing more datasets for protein-DNA interactions and proteomics-based approaches
318 may reveal more candidate factors for HSat3 and other satellites. Because many
319 nuclear factors are described as localizing to nuclear 'speckles' or 'bodies', it is likely
320 that a subset of these observations are explained by massive repetitive arrays enriched
321 for binding motifs.
322
323 The validated HSat3-binding factors are associated with a wide range of signaling
324 pathways and disease states, with no obvious shared functionality. While TEADs are
325 the effector of the Hippo pathway, NFAT members play important roles in T-cell
326 activation and development[36]. IRF3 drives the interferon expression following innate
327 immunity activation[37]. CUX1 is a broadly expressed repressor with specific roles in
328 neuronal development[38]. PRDM15 maintains naive pluripotency via WNT / MAPK-ERK
329 signaling pathways[32]. Thus, the precise functions of each potential TF-HSat3 interaction
330 need to be evaluated separately. We focused our attention on our top hit, the TEAD
331 family, given its well-studied roles in development, tissue homeostasis, and disease[39].
332
333 ***Endogenous TEAD1 binds HSat3***
334 TF binding to HSat3 could be exaggerated by overexpression, given the high density of
335 potential binding sites and the prior expectation that these regions are maintained in a
336 dense heterochromatic state. We therefore generated MCF10A cells in which we
337 tagged endogenous TEAD1 with eGFP to assess its localization to HSat3. Indeed,
338 confocal imaging revealed multiple TEAD1 foci in each cell nucleus (Figure 4a). The
339 largest foci likely correspond to the large HSat3 array on chromosome 9 (Figure 1a), as
340 this XX line does not have the large chromosome Y array. To confirm endogenous
341 TEAD1 foci are indeed binding HSat3, we generated metaphase spreads with MCF10A
342 TEAD1-egfp cells, probing with 488-Alexa conjugated anti-GFP nanobody (Figure 4b).
343
344 Both chromosome 9 copies showed pericentromeric staining, corresponding to HSat3
345 (MCF10A cells have a known chromosome 9 translocation, causing one copy to be
346 longer[40]). Further, there is clear TEAD1 signal on many of the HSat3-containing
347 acrocentric chromosomes (13-15, 21-22). Chromosome 15 in particular has an 8 Mb
348 HSat3 array, corresponding to the brightest TEAD1 signal on the acrocentrics. Finally,

Figure 4:

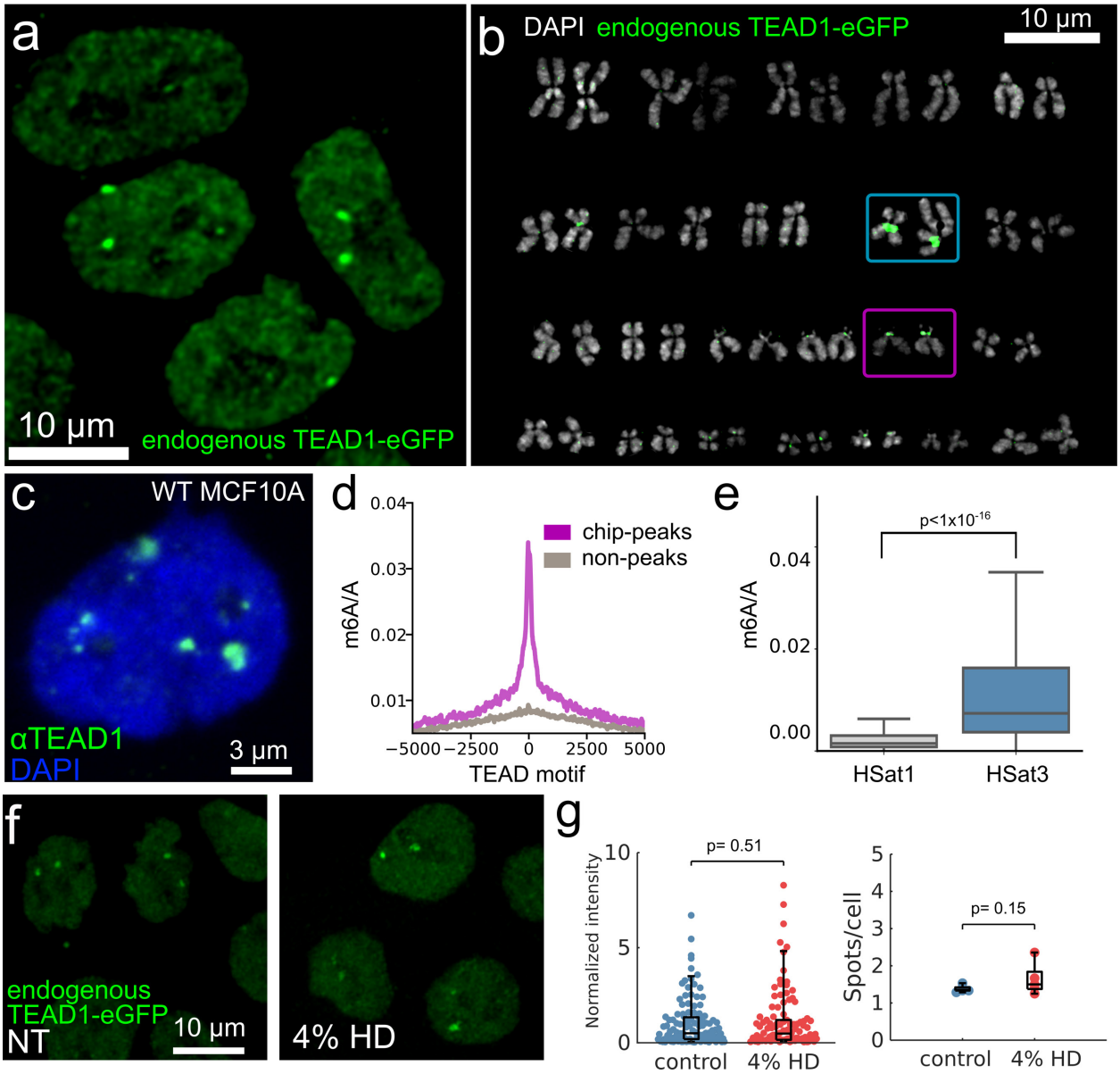

Figure 4: Endogenous TEAD1 binds HSat3. (a) TEAD1-eGFP knock-in (KI) at the endogenous locus in MCF10A cells shows clear sub-nuclear foci in live-cell microscopy. Image is a representative, single z-plane. (b) Representative metaphase spread of MCF10A with TEAD1-eGFP knock-in stained with GFP nanobody. The karyogram shows localization to the two largest HSat3 arrays (blue=chromosome 9, purple box=chromosome 15). To preserve TEAD1 signal, no other FISH or DNA stains could be used to generate banding patterns, thus chromosomes are organized by size as an approximation for the karyotype. MCF10A has a known translocation on chromosome 9[40], showing two distinct chromosome sizes. Consistent results were obtained in two other metaphase spreads. (c) Immunofluorescence for TEAD1 in WT MCF10A, showing untagged endogenous TEAD1 shows sub-nuclear foci in unfixed wildtype (WT) MCF10A nuclei isolated for DiMeLo-seq. Image is a representative single z-plane. (d) TEAD1-targeted DiMeLo-seq in WT MCF10A. m6A signal is normalized to A, and centered at TEAD1 motifs within known TEAD1 ChIP-seq peaks. As an internal control, the signal is plotted at 25,000 randomly selected TEAD1 motifs outside of known ChIP-seq peaks and not within HSat3. (e) Distribution

of m6A/A per read aligned to either HSat1 (N=668 reads) or HSat3 (N=1961 reads), showing specificity of TEAD1 binding to HSat3, as HSat1 is not enriched for TEAD motifs. The box plot lines are as follows: center line, median; box limits, upper and lower quartiles; whiskers, 1.5x interquartile range. A one-tailed Wilcoxon rank sum test was performed to compare m6A/A enrichment between HSat1 and HSat3. (f) Live-cell microscopy of endogenous TEAD1-eGFP in MCF10A in untreated and 10 minutes 4% 1,6-Hexanediol (HD) treatment showing no change in foci intensity or frequency. (g) Quantification of data from panel f. For the foci intensity comparison, Nfoci(control)=117, Nfoci(HD)=106. For number of foci per cell comparison: Ncells(control)=172, Ncells(HD) =141, with individual data points representing the mean for each region of interest. Image is a representative single z-plane. The experiment was performed twice, with similar results; data shown are from one biological replicate.

---

we performed immunofluorescence staining on unfixed, permeabilized, wildtype MCF10A nuclei using an anti-TEAD1 primary antibody and imaged using confocal microscopy. These nuclei showed bright TEAD1 foci (Figure 4c), suggesting that the TEAD1-eGFP tag used in other experiments does not introduce localization artifacts, and that TEAD1 remains strongly bound to HSat3 without fixation.

We further validated endogenous TEAD1 binding to HSat3 using anti-TEAD1 DiMeLo-seq in unfixed, wildtype MCF10A cells, yielding m6A enrichment at known TEAD1 binding sites (Figure 4d). Within the sample, we measured bulk enrichment of m6A/A in HSat3 compared to an average of HSat1-A and -B, which are distinct satellite repeat families also present on acrocentric chromosomes and not predicted to be bound by TEAD (Figure 4e).

Phase separation of TFs into condensates has been reported for various TFs, including endogenous YAP and TEAD1[41]. Because phase separation is highly dependent on concentration, the high-frequency motifs embedded in satellite DNA may seed phase-separation through increased local concentration, as proposed for HSF1[42]. To test whether the observed TEAD binding to HSat3 is driven by phase separation, we incubated cells with 4% 1,6-Hexanediol, but this did not dissolve endogenous TEAD1-eGFP foci in live cells or reduce foci intensity (Figure 4f-g). In summary, our data suggest that endogenous TEAD1 binds HSat3 primarily through motif recognition.

YAP localization to HSat3-bound TEAD depends on cellular state

TEAD-family factors require co-activators or co-repressors to regulate gene transcription. YAP is the best-characterized co-activator of TEADs. The YAP/TEAD complex mostly functions at gene enhancers, driving a transcription program that promotes cell proliferation[43]. Because TEAD1 appeared constitutively bound to HSat3, and YAP distributes well into the nucleus in interphase MCF10A[44], we hypothesized that YAP should readily bind TEAD1/HSat3 foci. Using previously generated MCF10A YAP-eGFP/TEAD1-mCherry KI cells[44], we did not observe increased YAP signal corresponding to the large TEAD1-HSat3 foci in interphase cells using 60X confocal

406 microscopy (Figure 5a,c). However, mitotic cells showed strong YAP colocalization to
407 TEAD1 foci (Figure 5b-c). Thus, the YAP/TEAD/HSat3 complex can form, but the
408 formation of large YAP foci is cell-state dependent.
409
410 To better understand regulation of YAP/TEAD on HSat3, we generated a series of YAP
411 truncations fused to mEGFP containing the YAP TEAD-binding domain (TBD) (Figure
412 5d). Because endogenous YAP was not readily localized to TEAD1 in interphase cells,
413 we employed live-cell super-resolution imaging with Zeiss Airyscan to assess
414 YAP(TBD) binding to TEAD/HSat3 foci. We observed frequent localization of YAP-TBD-
415 meGFP to sub-nuclear foci (Figure 5e-f). Whereas both YAP(TBD+WW1) or
416 YAP(TBD+WW1+WW2) decreased the frequency of sub-nuclear foci, with almost no
417 cells showing detectable YAP(TBD+WW1+WW2) foci (Figure 5e-f). These results
418 suggest the domains of YAP may regulate its ability to bind TEAD1/HSat3, as the WW
419 domains are responsible for multiple protein-protein interactions[45].
420
421 Given the known heterochromatic status of HSat3, we hypothesized that treatment with
422 Trichostatin A (TSA), a potent HDAC class I/II inhibitor, would de-condense HSat3
423 heterochromatin. Treatment of MCF10A cells with TSA led to a dramatic increase in
424 YAP localization to sub-nuclear foci (Figure 5g-h). To our surprise, we found small
425 nucleolar YAP foci in untreated cells using Airyscan (Figure 5g).
426
427 We thus hypothesized that endogenous YAP/TEAD1 binding to HSat3 does occur in
428 interphase MCF10A , but foci were not detectable using 60X confocal microscopy.
429 Although YAP is generally excluded from the nucleolus, we observed frequent nucleolar
430 foci (Supplementary Figure 14). To prove these are indeed TEAD-bound HSat3, we
431 generated a dual knock-in of endogenous TEAD1-HALO and YAP-eGFP in MCF10A.
432 Indeed, nucleolar foci always colocalized with TEAD1-HALO stained with HALO-tag
433 JF647 dye (Supplementary Figure 15), and all TEAD-family members colocalize 1:1
434 with ZFsat3, including foci within the nucleolus (Supplementary Figure 8). This is
435 consistent with the genome organization of rDNA-containing acrocentric chromosomes,
436 where HSat3 arrays are found on both sides of the nucleolar organizing regions (i.e.
437 rDNA repeats plus distal- and proximal-junctions) (Supplementary Figure 16).
438
439 The presence of non-ribosomal DNA localization within the nucleolus has not been
440 thoroughly explored. For example, we found only one decades-old report describing
441 satellite DNA inside the nucleolus using DNA FISH[46], whereas previous work typically
442 describes satellite DNA as perinucleolar[47]. This lack of prior observations may be due to
443 fixation artifacts and limits of resolution, as live-cell, super-resolution imaging of satellite
444 DNA localization has not previously been reported, to the best of our knowledge.

Figure 5:

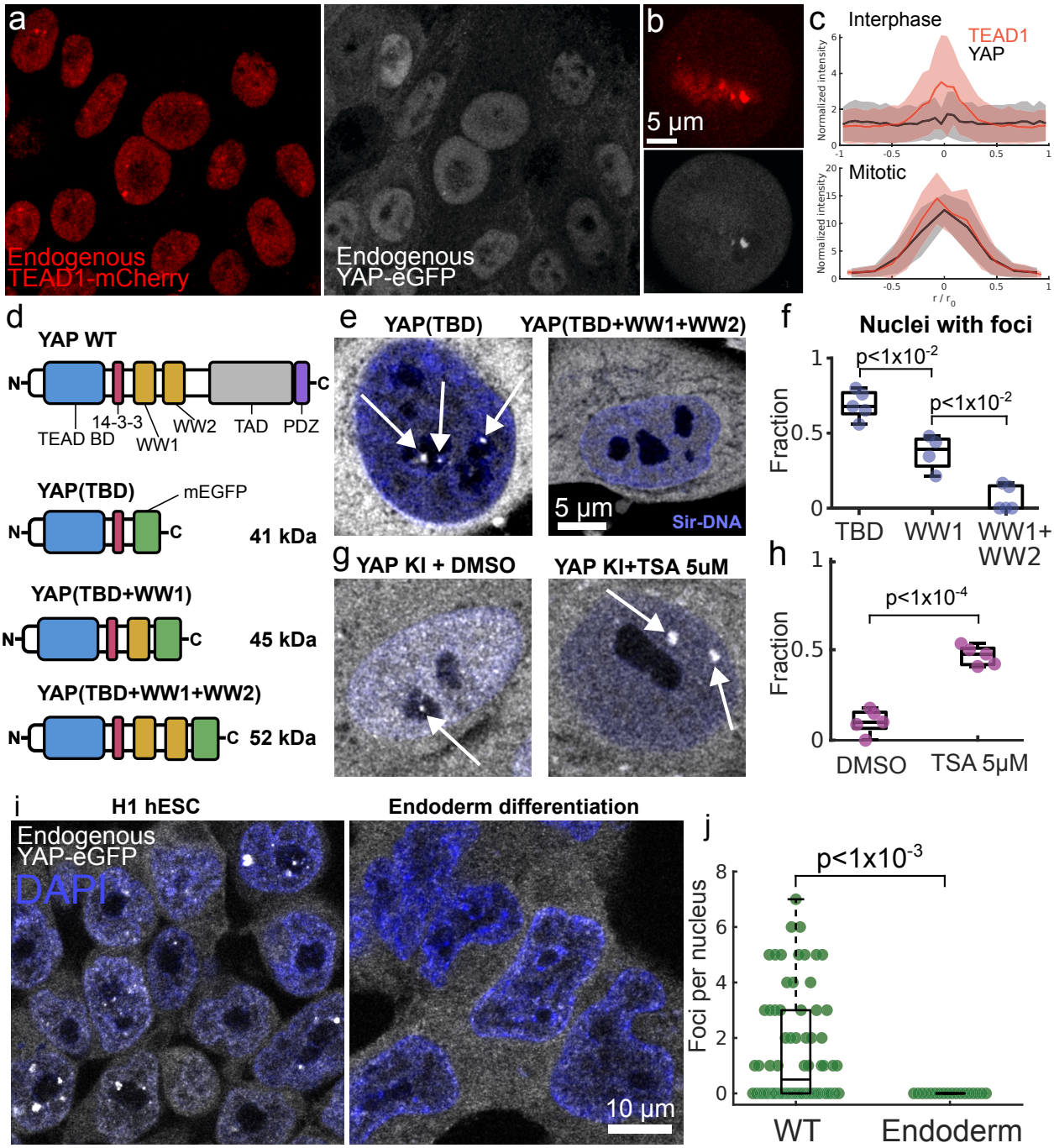

Figure 5: Cell-state dependent regulation of YAP binding to TEAD1/HSat3. (a-b) Two-color imaging of endogenous TEAD1-mCherry and YAP-eGFP shows no significant colocalization at HSat3 foci in interphase cells, and strong colocalization in mitotic cells. (c) Intensity analysis of images from panels a-b. For interphase cells, The TEAD1-mCherry intensity profile was generated from 23 foci detected from 55 cells. The YAP-eGFP intensity profile was generated by querying the TEAD1 foci pixels in the GFP channel. For mitosis, a representative cell was used to generate the intensity profile using the brightest TEAD1 focus. Shaded region represents the standard deviation. Experiment was performed three times with similar results. (d) Diagrams of YAP protein domains. Blue: TEAD binding domain (TBD), Red: 14-3-3 binding domain, Yellow: WW1 and WW2 domains, grey: transcription activation domain (TAD), purple:

PDZ domain. YAP truncations fused to mEGFP and their molecular weights are shown. (e-f) live-cell super-resolution imaging shows frequent YAP(TBD) sub-nuclear foci which are nearly absent in YAP(TBD+WW1+WW2). Cells were stained with Sir-DNA for a live-cell nuclear marker. The fraction of cells with at least one detected focus are shown in (f). The number of cells per condition are as follows: N(TBD)=130, N(WW1)=90, N(WW1+WW2) = 52. Individual data points represent mean per ROI. Significance was assessed by one-tailed t-tests. Repeated two to three times with similar results. (g) Live-cell microscopy of endogenous (i.e. full length) YAP-eGFP knock-in (KI) treated with 5 μM Trichostatin A or DMSO, and stained with Sir-DNA. Treated cells show YAP localization to large sub-nuclear foci. (h) The fraction of cells with at least one detected sub-nuclear focus. The number of cells per condition are as follows: N(DMSO)=165, N(TSA)=106. Individual data points represent mean per ROI. Significance was assessed by a one-tailed t-test. Repeated twice with similar results. (i) Live-cell microscopy of H1 hESCs with endogenous YAP-eGFP stained with Sir-DNA. Untreated H1 cells frequently show many YAP foci which are immediately lost upon Activin A treatment to promote endoderm differentiation. (j) The foci count per cell nucleus is plotted for WT and endoderm differentiated cells. The number of cells per condition are as follows: N(WT) =72, N(endoderm)=18. A one-tailed Wilcoxon rank sum test was performed to assess statistical significance between conditions. Experiment performed twice with similar results; data shown is from one biological replicate.

Reports using dCas9 have shown the large chromosome 9 loci[25], but not the smaller HSat3 arrays shown in our study.

Embryonic stem cell chromatin is largely euchromatic, whereas differentiation drives cell-type specific heterochromatin formation. This trajectory is also true for repetitive elements[48]. We next asked if HSat3 was more physically accessible to YAP/TEAD binding in hESCs. Using endogenous YAP-eGFP KI in H1 hESCs, we observed persistent large nuclear YAP foci in most interphase cells (Figure 5i-j). Whereas definitive endoderm (DE) differentiation led to immediate loss of detectable nuclear YAP foci (Figure 5i-j), despite ample nuclear YAP localization.

In summary, our results imply that the heterochromatic nature of HSat3 decreases YAP/TEAD interaction on HSat3. However, small nucleolar TEAD/HSat3 arrays are readily accessible to YAP in terminally differentiated MCF10A cells. Surprisingly, mitotic chromosomes permit ample YAP/TEAD/HSat3 interactions, despite being in a condensed state. This may be explained by multiple reports of chromatin accessibility in mitosis where TFs ‘bookmark’ gene promoters and enhancers, despite the large-scale condensation of chromatids[49,50]. Previous work showed fast and strong silencing of rRNA transcription following DE differentiation of hESCs[51], which correlates well with the observed loss of nuclear YAP foci in hESCs upon DE differentiation. We thus hypothesized that HSat3 adjacent to rDNAs may regulate RNA Polymerase I (Pol-I) transcription via YAP/TEAD.

Exogenous expression of YAP and the paralogue TAZ has previously been reported to induce compartmentalization of TEAD-family factors, whereas TEAD did not localize to

499 phase-separated compartments on its own[52,53]. However, a recent report demonstrated
500 the localization of FLAG-TEAD4 to sub-nuclear compartments. These inconsistent
501 observations may be due to immunofluorescence and/or fixation artifacts, as unfixed
502 immunofluorescence showed consistent sub-nuclear endogenous TEAD1 foci (Figure
503 4c). Our results highlight the need to endogenously tag YAP and TEAD for live-cell
504 imaging to avoid overexpression and immunofluorescence artifacts.
505
506 ***YAP/TEAD/HSat3 regulate rDNA transcription in the nucleolus***
507 The Hippo pathway acts as a global regulator of cell growth by sensing intracellular and
508 extracellular cues, including GPCR-ligands, extracellular matrix mechanics,
509 temperature, and metabolic states[16]. This pathway shows sensitivity to signaling inputs
510 on a timescale of minutes[44,54,55], providing a rheostat-like mechanism for regulating cell
511 proliferation. Ribosome biogenesis represents a massive energy demand for the cell.
512 rRNA genes are the most highly transcribed genes, representing 80-90% of total RNA in
513 cells[56].
514
515 In humans, not only are all rDNA arrays surrounded by multiple HSat3 arrays (Figure
516 1a), the homologues of human chromosomes 9 and Y in orangutans contain rDNA
517 arrays adjacent to HSat3 (Supplementary Figure 16)[9,57]. Further, all rDNA-containing
518 chromosomes in great apes contain nearby HSat3 arrays (Supplementary Figure 16),
519 suggesting a well-conserved relationship between these two elements. Given the known
520 roles of the Hippo pathway, and localization of YAP/TEAD to HSat3, we hypothesized
521 that YAP/TEAD activity may regulate rRNA synthesis. Although the YAP/TEAD complex
522 is only known as a RNA Polymerase II (Pol-II) regulator, many canonical Pol-II TFs
523 directly regulate rDNA transcription, including cMYC[58] and CEBPα[59].
524
525 In MCF7 TEAD1-4 knock-out cells[60], we found a 31% reduction in total RNA/DNA
526 compared to wildtype MCF7 cells, suggesting that YAP/TEAD activity is upstream of
527 rRNA transcription (Figure 6a). However, this effect could be due to global loss of
528 YAP/TEAD activity, not necessarily through direct regulation of RNA Pol-I activity.
529
530 We hypothesized that HSat3 arrays act as enhancer-like elements for RNA Pol-I
531 transcription via YAP/TEAD. To test this, we generated a RNA Pol-I enhancer construct
532 consisting of the rDNA Upstream Control Element (UCE) and core promoter, followed
533 by an IRES-meGFP-polyA expression cassette, and downstream Transcription
534 terminator 1 (TTF1) sites (Figure 6b). To test the effects of HSat3 on RNA Pol-I
535 transcription, we inserted either a 1.8 kb HSat3 element containing 104 GGAATG motifs
536 (i.e. canonical TEAD binding sites), or a 1.8 kb neutral element from the human PAWR

537 **Figure 6:**

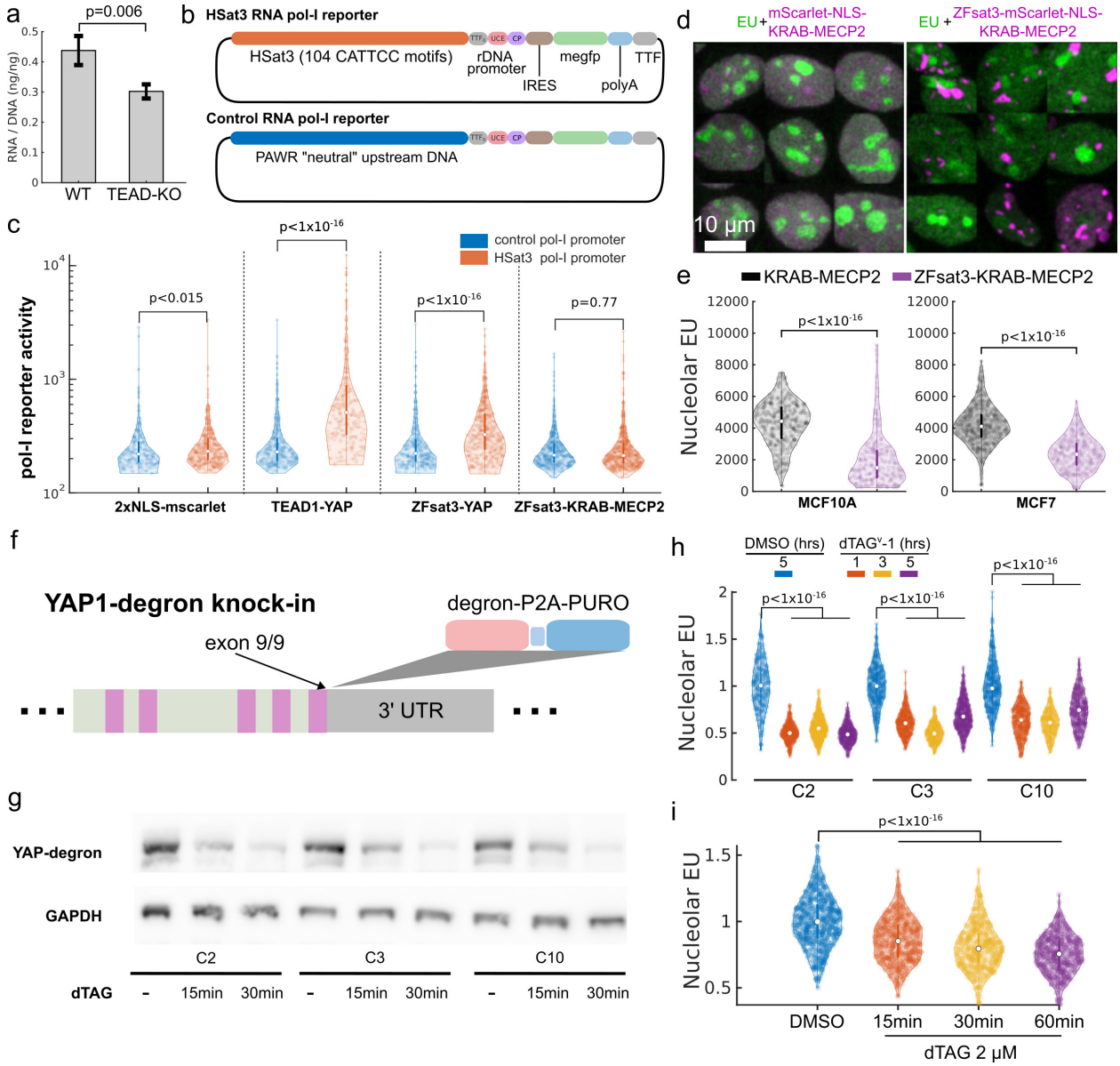

538

539 **Figure 6: YAP positively regulates RNA Pol-I activity.** (a) Permanent TEAD KO in MCF7 cells led to
540 reduced RNA/DNA ratios. Bar plot generated from 3 biological replicates. Bar plot error represents
541 standard deviation. Statistical significance was assessed using a one-tailed T-Test. (b) Design of RNA
542 Pol-I reporter constructs with either HSat3 elements containing 104 CATTCC sites, or an equivalent-
543 length DNA segment from the human PAWR gene. (c) Results of RNA Pol-I reporter assays. 293T cells
544 were transfected with either control or HSat3-Pol-I reporters and 2xNLS-mScarlet (non-activating),
545 TEAD1-mScarlet-YAP fusion, ZFsat3-mScarlet-YAP fusion, or ZFsat3-mScarlet-KRAB-MECP2. Cells
546 were segmented using the nuclear mScarlet, and GFP signal was quantified from the cytoplasm of
547 segmented cells. The number of cells per condition are as follows: N(control+NLS-mscarlet)=270,
548 N(HSat3+NLS-mscarlet)=496, N(control+TEAD-YAP)=369, N(HSat3+TEAD-YAP)=275,
549 N(control+ZFsat3-YAP)=358, N(HSat3+ZFsat3-YAP)=561, N(control+ZFsat3-KRAB-MECP2)=514,
550 N(HSat3+ZFsat3-KRAB-MECP2)=720. A one-tailed Wilcoxon rank sum test was performed to assess
551 statistical significance between control and HSat3 reporter activity. (d) representative confocal microscopy
552 images of EU assay with MCF10A cells expressing either mScarlet-NLS-KRAB-MECP2 (KM) or ZFsat3-

mScarlet-NLS-KM (ZFsat3-KM). Image is constructed by tiling 9 representative nuclei within each condition. (e) Quantification of nucleolar EU fluorescence intensity in MCF10A and MCF7 cells stably expressing ZFsat3-mScarlet-KM and mScarlet-KM. The number of nucleoli per condition are as follows: N(MCF10A KRAB-MECP2)=447, N(MCF10A ZFsat3-KRAB-MECP2)=270, N(MCF7 KRAB-MECP2)=1729, N(MCF7 ZFsat3-KRAB-MECP2)=945. A one-tailed Wilcoxon rank sum test was performed to assess statistical significance between KM and ZFsat3-KM. (f) Diagram depicting knock-in of degron-p2a-puromycin cassette at the human YAP1 locus. (h) 1 hr EU incorporation assay for H1 hESC YAP-degron clonal cell lines treated with DMSO or 2 μM dTAGv1 at various times. The number of nucleoli per condition are as follows: N(DMSO C2)=277, N(dTAG 1hr C2)=446, N(dTAG 3hr C2)=557, N(dTAG 5hr C2)=477, N(DMSO C3)=446, N(dTAG 1hr C3)=494, N(dTAG 3hr C3)=393, N(dTAG 5hr C3)=629, N(DMSO C10)=485, N(dTAG 1hr C10)=484, N(dTAG 3hr C10)=346, N(dTAG 5hr C10)=414. (i) 1hr EU incorporation assay for H1 hESC YAP-degron clone 2 after 15, 30, and 60 min dTAGv1 treatment. N(DMSO)=854, N(dTAG 15 min)=577, N(dTAG 30 min)=560, N(dTAG 60 min)=548. Data represents one biological replicate. The experiment was performed twice with similar results.

---

gene devoid of TEAD binding sites ahead of the rDNA promoter. The reporter was sensitive to both actinomycin D and an RNA Pol-I inhibitor Bmh-21 (Supplementary Figures 17-18). Co-transfecting the reporter and a 2xNLS-mScarlet expression plasmid showed a minor change in activity between the control and HSat3 rDNA reporters (Figure 6c). However, co-transfecting a chimera gene consisting of the TEAD1 DNA binding domain and the transcription activating domain (TAD) of YAP (TEAD-YAP) strongly increased the activity of the HSat3 rDNA reporter, but not the control rDNA promoter (Figure 6c). Similarly, co-transfecting ZFsat3-YAP activated the HSat3 rDNA reporter, but to a lesser extent. This is potentially due to reduced stoichiometry as each ZFsat3 targets 18 bp, compared to the TEAD1 footprint which is closer to 6 bp. To test the specificity of YAP activation of RNA Pol-I, we generated a TEAD1 fusion to VP64, a generic potent RNA Pol-II activator. TEAD1-VP64 did not activate the rDNA promoter, demonstrating the YAP transcription activation domain is specifically activating the RNA Pol-I reporter (Supplementary Figure 19).

The genetic deletion of all rDNA-adjacent HSat3 arrays cannot be done due to the sheer number of individual arrays (Supplementary Figure 1). Further, compensatory mechanisms may develop during clonal selection of HSat3-deleted cells. Therefore, we targeted HSat3 directly with a KRAB-MECP2 (KM) repressor[61] fused to ZFsat3-mscarlet (ZFsat3-KM). The transcription rate of rRNA can be accurately quantified using incorporation of an ethynyl modified uridine analog (5-Ethynyluridine, EU), which shows strong nucleolar signal proportional to rRNA transcription[62]. In both MCF10A and MCF7, ZFsat3-KM showed strong inhibition of rRNA transcription compared to expression of KM alone (Figure 6d-e) or ZFsat3-mScarlet alone (Supplementary Figure 20). In some cases with high ZFsat3-KRAB-MECP2 expression, cells showed almost no incorporation of EU in nucleoli (Figure 6d). This result suggests that the chromatin status of HSat3 is important for normal rRNA transcription.

596 We surmised the connection between rRNA transcription and YAP/TEAD/HSat3 is
597 strongest in hESCs, given the ample localization of YAP to nuclear foci in most cells
598 (Figure 5i). We generated clonal hESC lines with homozygous endogenous YAP-
599 degron KI (Figure 6f, Supplementary Figure 21), allowing acute degradation of YAP
600 (Figure 6g). All clones showed strong reduction of nucleolar EU signal following 1, 3,
601 and 5 hr degradation of YAP followed by 1 hr EU incorporation (Figure 6h). We further
602 probed EU incorporation after 15, 30, and 60 minutes of YAP degradation for clone 2.
603 This showed detectable EU reduction even after 15 minutes of YAP degradation
604 followed by 1 hr of EU incorporation (Figure 6i). We measured a ~25% drop in rRNA
605 transcription rate after 1 hr of YAP degradation plus 1 hr EU incorporation, however, it is
606 possible that the YAP paralogue TAZ or other HSat3-bound TFs are compensating for
607 loss of YAP. In comparison, degradation of degron-tagged CEBPα, which directly binds
608 the rDNA promoter, showed a ~7% decrease in rDNA synthesis after 2 hours of
609 dTAGv1 treatment, measured using FISH against nascent rRNA[59]. The speed and
610 magnitude of reduction in rDNA synthesis after acute degradation of YAP implies a
611 direct relationship, although second-order effects cannot be formally ruled out.
612
613 Because HSat3 arrays are found adjacent to all rDNA arrays, we hypothesized that
614 YAP/TEAD/HSat3 may be co-localized with UBTF, a core rDNA TF that marks active
615 rDNAs (Figure 7a). Two-color imaging of mScarlet-UBTF and endogenous YAP-eGFP
616 in H1 hESCs showed 58% of YAP foci contacting UBTF foci within nucleoli (Figure 7b).
617
618 Together, these results show YAP/TEAD/HSat3 not only co-localizes with rDNA
619 machinery in live cells, but it can directly activate the rDNA promoter (Figure 7c). Thus,
620 we propose two possible models: (1) The YAP/TEAD complex on HSat3 forms 3D
621 interactions with rDNA in the nucleolus, or (2) TEAD/HSat3 increases the nucleolar
622 concentration of YAP, allowing more frequent contacts with the rDNA promoter.

Figure 7:

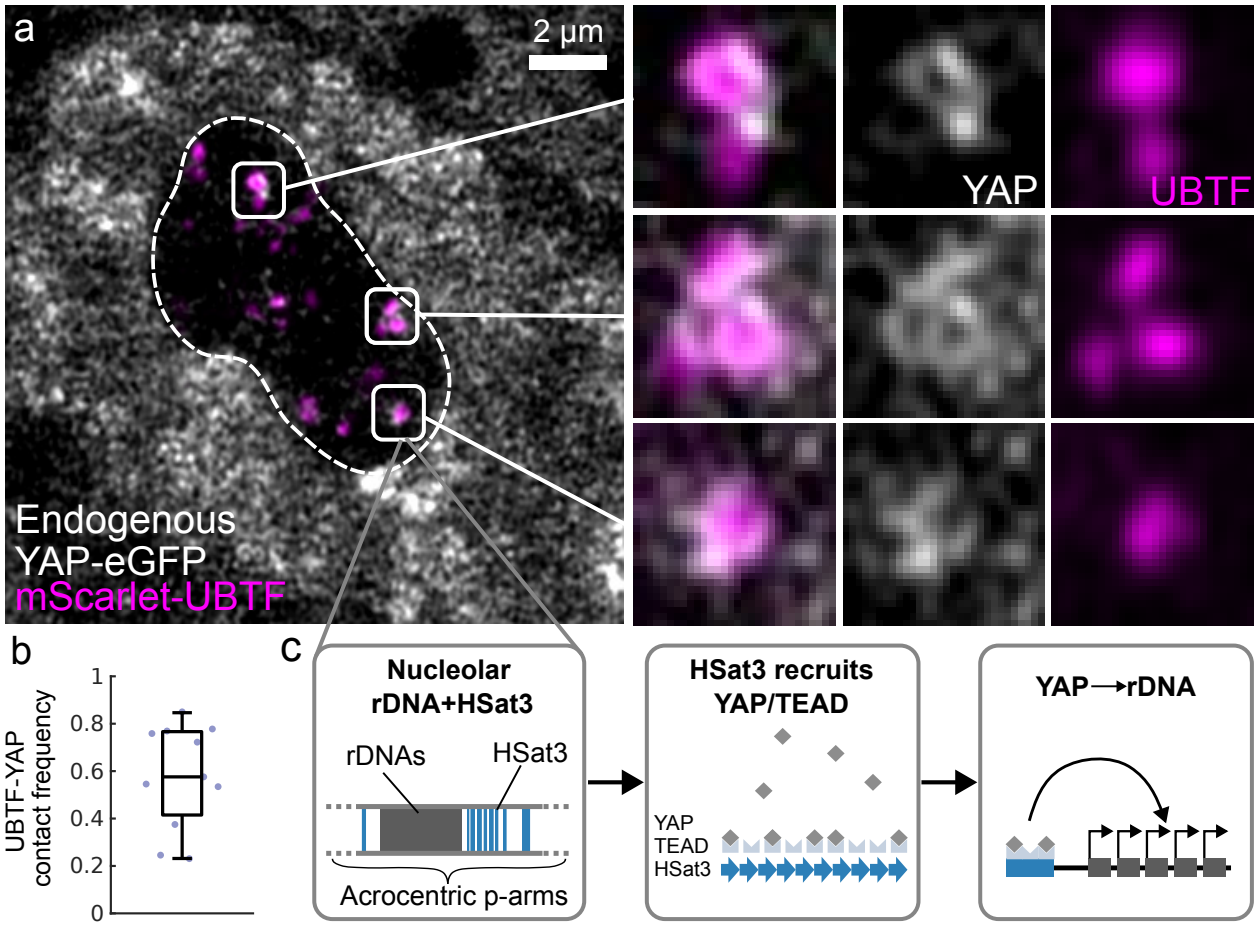

Figure 7: Colocalization of YAP and UBTF in nucleoli. (a) Live-cell super-resolution imaging (Airyscan) of mScarlet-UBTF and endogenous YAP-eGFP in H1 hESCs. Dashed line represents the outline of the nucleolus. Insets show contact between UBTF foci and YAP foci. (b) Nucleolar UBTF and YAP foci are segmented, and the fraction of UBTF foci that touch YAP foci is quantified per cell. Data points represent mean contact frequence per cell (N=11 cells, with a total of (c) Summary of the major findings presented in this work. Left: Detection of nucleolar HSat3. Center: endogenous TEAD binds HSat3 and recruits YAP. Right: YAP regulates RNA Pol-I activity.

633 **DISCUSSION**
634
635 Our work has unveiled a set of novel HSat3-binding TFs, many of which have potent
636 transcription driving functions. These TFs function in various signaling contexts,
637 including development, immune response, T-cell activation, and human cancers. Our
638 findings suggest that constitutive heterochromatin contains a diverse and dynamic
639 collection of proteins[63,64], rather than being an inert or purely repressive monolith[65].
640 Characterizing the complete set of satellite binding TFs and their functions may add to
641 this growing body of previously unappreciated protein-DNA interactions.
642
643 We further explored the potential biological functions of our findings by focusing on
644 TEAD, which is widely expressed as part of the Hippo pathway and normally plays a
645 role in cell proliferation. We observed HSat3-bound TEAD foci within nucleoli, along with
646 TEAD's co-activator YAP co-localized with the RNA Pol-I transcription factor UBTF. We
647 thus hypothesized that YAP/TEAD may play a direct role in rDNA regulation, mediated
648 by binding to HSat3, given the well-documented functions of the Hippo pathway as a
649 growth control network. Acute degradation of YAP revealed a rapid decline in
650 endogenous rDNA transcription, and the YAP transcription activation domain directly
651 activated an RNA pol-I reporter, confirming that YAP can promote RNA Pol-I activity in
652 cis. Lastly, recruitment of a KRAB-MECP2 repressor to HSat3 led to strong inhibition of
653 rDNA transcription, confirming that factors bound to HSat3 can influence RNA Pol-I
654 activity.
655
656 Because HSat3 arrays and rDNA arrays are often hundreds of kilobases apart, HSat3-
657 bound YAP/TEAD and rDNAs may directly interact via physical proximity within the
658 nucleolus. Alternatively, because co-activator binding is transient and dynamic, HSat3-
659 bound TEAD may simply increase the local concentration of the co-activator YAP,
660 enhancing rDNA expression at a distance. Future experiments will need to resolve this
661 question and further explore the precise mechanism by which YAP modulates rDNA
662 activity. Improved genetic tools may allow for the mutation/deletion of the satellite DNA
663 itself, though this remains extremely challenging given the large number and size of
664 satellite DNA arrays across many chromosomes throughout the genome.
665
666 To the best of our knowledge, human satellite DNAs, TEAD, and YAP have not
667 previously been observed inside the nucleolus, likely due to a lack of suitable super-
668 resolution live-cell imaging assays. A recent report described sub-nuclear TEAD4
669 condensates in live-cell imaging, which are dramatically enriched following glucose
670 starvation[66]. Although the genomic basis of these foci was not investigated, our results
671 suggest these are indeed HSat3-bound TEAD. We predict that the YAP paralogue TAZ
672 may operate on HSat3-bound TEAD in a similar manner to YAP. Because TAZ has

673 overlapping and distinct expression and cellular functions [67,68], further investigations in
674 cell types with strong TAZ activity may provide insights into the differential regulation of
675 rDNA by YAP and TAZ. Hypothetically, the relationship between satellite DNA and
676 rDNA regulation may extend beyond HSat3 and YAP/TEAD. Here, we propose a model
677 in which upstream regulators of rDNA transcription are brought into the nucleolus via
678 adjacent satellite repeats. Multiple IRF family members were previously found to directly
679 bind the rDNA promoter in human and mouse cells[59]. In our work, we demonstrated
680 IRF3 binding to HSat3, further supporting the notion that pools of rDNA-regulating TFs
681 are locally enriched via satellite DNA repeats.
682
683 Large HSat3 arrays appear to have originated adjacent to rDNA, as they are found
684 consistently on rDNA-containing chromosomes across great apes[9]. Human
685 chromosomes 9 and Y have the largest amount of HSat3 per chromosome, yet no rDNA
686 arrays. However, the homologous chromosomes in orangutan, the most distantly
687 related great ape, do harbor rDNA arrays[9,57]. This raises interesting questions about the
688 potential role of the HSat3-Hippo-rDNA regulatory axis in the evolution of great apes.
689
690 The recruitment of TFs like TEAD to HSat3 may change the underlying chromatin state.
691 Future studies will need to explore the effects of these TFs on phenomena like
692 chromatin compaction, histone modifications, HP1 association, and satellite
693 transcription. If TF-loaded satellite arrays have a less repressive chromatin state, they
694 may help to insulate highly active rDNAs from the surrounding repressive
695 heterochromatin. Our work suggests that upstream activation of the Hippo pathway
696 would reduce YAP-TEAD/HSat3 loading by YAP phosphorylation[16], shifting HSat3
697 towards a more repressive state and reducing rDNA transcription.
698
699 YAP/TAZ are implicated in a variety of human cancers[16]. The high metabolic demand of
700 tumor growth requires ample ribosome biogenesis, and thus rRNA transcription[69].
701 Further studies on oncogenic YAP/TAZ activation may reveal an underlying connection
702 to rRNA transcription via our proposed model. Overexpression of activated YAP induces
703 transcription of ribosomal protein components[70], and increases global translation even
704 during serum starvation[71]. In line with our results, we propose that YAP promotes rRNA
705 synthesis directly to meet increased translation demands induced by its own
706 downstream activities.
707
708 In summary, we have identified multiple, highly conserved transcription factors that
709 directly bind massive, poorly understood satellite repeats in the human genome. Our
710 results suggest one potential function of these satellite arrays is to act as enormous
711 gene regulatory elements that can modulate rDNA expression via TF enrichment in the
712 nucleolus.

713 **METHODS**
714
715 **Cell culture:**
716 293T: 293T cells (ATCC CRL-3216) were cultured in DMEM base media with 10% FBS,
717 1xPEN/STREP supplement. For transfections, Lipofectamine 3000 (Thermo Fisher Cat
718 L3000001) was used according to the manufacturer's instructions.
719
720 MCF10A: MCF10A cells were cultured as previously described[44].
721
722 H1 hESC: H1 cells were obtained directly from WiCell at passage 22. Cells were
723 cultured according to WiCell's protocol using Matrigel coating (Corning 354277),
724 mTESR Plus (Stem Cell Technologies 100-0276) and Versene EDTA (Fisher Scientific
725 A4239101). Briefly, cell culture surfaces were coated with Matrigel for 2 hrs or longer at
726 37 C in the tissue culture incubator. For passaging, cells were rinsed with once
727 Versene, incubated with Versene for 8.5 minutes at room temperature. Versene was
728 aspirated, and then fresh mTESR Plus media was used to lift hESC colonies from the
729 dish. Endoderm differentiation was carried out by washing once with DPBS, and
730 culturing with 50 ng/mL Activin A (Gibco Cat. No. PHC9564) with 3μM CHIR99021
731 (Selleck Chemicals Cat. No. S2924) in RPMI 1640 base media, replacing media once
732 after 24 hrs.
733
734 Stem cell Ethics statement: H1 hESC's were cultured in vitro in accordance with the
735 Stem Cell Research Oversight Panel (SCRO) which complies with federal, state and
736 Stanford policies.
737
738 For transient transfections, cells were passaged using Accutase (Stem Cell
739 Technologies 07920) to generate single-cell suspensions, followed by seeding with
740 Revitacell Supplement (Fisher Scientific A2644501). The next day, cells were
741 transfected with Lipofectamine Stem Cell reagent (Invitrogen STEM00015) following
742 manufacturers instructions.
743
744 **HSat3 motif analysis:**
745 Karyoplot of HSat3 arrays in the human genome was made using the
746 centromere/satellite annotations of T2T-CHM13v2.0 and karyoplotteR package in R.
747
748 To calculate the enrichment of TF motifs across Hsat3, we used the MEME-Suite tool
749 SEA: Simple Enrichment Analysis. Background sequences were generated from T2T-
750 CHM13v2.0 reference genome using the 2000 bases upstream of 5000 randomly
751 selected genes from NCBI ref seq annotation. For each selected gene, ten 50-base pair
752 sub-strings were randomly chosen, providing 50,000 "reads" for background data. The

753 input sequences were similarly generated from HSat3 annotations designated by sub-
754 family[1]. Because HSat3 is inherently repetitive, we generated substrings with a mean
755 length of 50 base pairs with standard deviation of 4 to avoid biasing. For each HSat3
756 element, the complete set of 50+/-4 base pair strings were used for SEA analysis. For
757 TF motifs, we used the JASPAR 2024 database
758 (https://jaspar.elixir.no/download/data/2024/CORE/JASPAR2024_CORE_non-
759 redundant_pfms_meme.txt). A heat-map was generated using a custom python script,
760 plotting the enrichment values from SEA. We clustered individual HSat3 arrays by
761 subfamily (A1,B2,B6, etc) using Ward hierarchical clustering with Euclidean distance
762 (scipy.cluster.hierarchy). Raw data and scripts will be available upon publication.
763
764 **ChIP-seq screen:**
765 We downloaded publicly available ChIP-seq data from the ENCODE portal to mine for
766 putative HSat3-binders. The ENCODE cell lines included in this screen are: HepG2,
767 WTC11, H1, HCT116, A549, GM23338, K562, HEK293, GM12878, MCF-7, HEK293T,
768 SK-N-SH, and IMR-90. We screened a total of 2,407 ENCODE accessions, ensuring
769 each had at least one experimental and one control dataset, with most accessions
770 containing at least two replicates. Data were specifically split between male and female
771 cell lines to account for sex-specific differences, and only accessions with paired control
772 datasets were downloaded. This resulted in 13,542 FASTA files that were downloaded
773 and aligned to the Chm13v2.0 genome with or without chromosome Y depending on
774 cell line sex. Alignment was carried out using BWA[72]. We added an additional dataset
775 for HSF1 ChIP-seq in Heat-shocked MCF7 cells as a positive control (GSE209667).
776
777 To calculate the enrichment ratio of transcription factor binding in satellite regions, we
778 defined control regions as 2,000 randomly sampled windows of 100 kilobases each
779 across the genome. For female cell lines, chromosome Y was excluded. The mean
780 number of reads in these control regions was calculated for each sample and used as
781 the denominator to normalize for antibody and ChIP biases inherent in the datasets.For
782 each sample, both control and experimental, we calculated the ratio of reads in the
783 satellite region to the mean reads in the control regions. To measure the effect size, we
784 took the median of these ratios for all experimental datasets corresponding to a given
785 cell line, transcription factor, and satellite DNA. This median was then divided by the
786 median ratio obtained from the control datasets for the same sample parameters.
787 Statistical significance was assessed using the Mann-Whitney U test to compare the
788 effect sizes between control and experimental groups with the null hypothesis that the
789 satellite regions have less or equal transcription factor binding compared to the control
790 regions.
791
792

Library of HSat3-binding TFs:

Starting with a lentivirus vectors pHIV-EF1alpha-mcs-pgk-puro/hygro, we generated base constructs for N-spytag3-mScarlet-linker-X or X-linker-mScarlet-spytag3-C tagging of genes, where X is a restriction site for inserting arbitrary cDNAs via NEB HiFi assembly. Most TFs were sourced from the Multiplexed Overexpression of Regulatory Factors (MORF) Library, a gift from Feng Zhang (Addgene #1000000218). TFs not available within the library were amplified directly from cDNA. Base constructs, TF-expressing constructs, sequences and primers used to PCR TFs are found in Supplementary data (provided after publication).

TF cDNAs were PCR amplified using NEB Q5 2x mastermix (NEB Cat. No. M0541L) and gel-purified using Qiagen gel purification kit (Qiagen Cat. No. 28704). Assembly of each factor was done using NEB HiFi 2X mastermix (NEB Cat. No. E2621L) with 50 ng of digested backbone and 10-40ng of gel purified cDNA following standard protocol from NEB. Assembled constructs were transformed into NEB DH5alpha (NEB Cat. No. C2987H). All clones were validated by long read sequencing (Plasmidsaurus).

Lentivirus particles were generated for TF expression constructs using Pspax2 / pmd2.g (gift from Addgene). using 293T cells. Briefly, [transfection mix] in 6-well plates coated with poly-L-lysine (Millipore Cat. No. A005C). Virus containing supernatant was concentrated 100-fold using Lenti-X Concentrator (Takara bio Cat. No. 631231), and used immediately or frozen at -80 C.

293T cells were transduced with lentivirus and polybrene at 10 µg/mL (Millipore Cat. No. TR-1003-G), and selected using puromycin at 2.0ug/mL, or hygromycin B at 200 ug/mL.

Design and validation of HSat3 Zinc Finger array:

The original design of the HSat3 Zinc-Finger (ZFsat3) was done using a now defunct webtool (https://www.scripps.edu/barbas/zfdesign/designzf.php). However, the design principles are described in Wright et al[73]. An optimal protein sequence was obtained by targeting an 18-bp perfect HSat3 repeat target [5'-GGAAT-GGAAT-GGAAT-GGA-3']. The resulting amino acid sequence including ZFs and linkers will be released upon publication.

The human codon optimized gene was generated by Twist Biosciences, and cloned into a pHIV backbone with an EF1 alpha promoter using restriction cloning. The ZFsat3 was cloned with a linker, mScarlet, and NLS at the C-terminus. Plasmid sequence available in the supplementary materials.

832 We validated the specificity of ZFsat3 binding to HSat3 using immuno-FISH. MCF10A
833 cells were infected with lentivirus encoding ZFsat3-mScarlet-NLS, and selected using
834 puromycin at 1µg/mL. After antibiotic selection, 20,000 cells were plated on Mattek
835 imaging dishes (Mattek Cat. No. P35G-1.5-10-C). Dishes were pre-coated with human
836 Fibronectin (Corning Cat. No. 356008) at 10 µg/mL for 1 hr at room temperature. Cells
837 were rinsed once in DPBS, and fixed with 4% paraformaldehyde in DPBS for 15
838 minutes at room temperature. Fixed cells were permeabilized by three washes of 3
839 minutes each with 0.1% Triton X-100, and blocked for 1 hour with 3% BSA in PBS.
840 Direct immunofluorescence was performed with anti-RFP antibody (Rockland
841 Immunochemicals, Cat. No. 600-401-379) labeled with CF488 fluorescent dye using
842 Biotium Mix-N-Stain (Biotium Cat. No. #92233), at 0.57 µg/mL for 1 hour at room
843 temperature. Samples were then washed three times for 5 minutes in PBS, followed by
844 post-IF fixation with 1% PFA for 10 minutes and three 1 minute PBS washes, and 10
845 minute aldehyde quenching with 20mM glycine in PBS.
846
847 For HSat3 DNA FISH, the samples were then incubated in 25% glycerol in PBS for 1
848 hour at room temperature, followed by three liquid nitrogen snap freeze-thaw cycles.
849 Typical FISH protocols require 0.1 M HCl treatment to improve FISH probe penetration,
850 which would bleach the dye-labeled RFP antibody. Instead, samples were lightly
851 digested with DNAse-I (Ambion Cat. No. AM2222) at 0.5 U/mL for 5 minutes at room
852 temperature followed by inactivation with EDTA at 2mM final concentration. The buffer
853 was then exchanged to 50% formamide with 2X SSC (Invitrogen 20X SSC Cat. No.
854 AM9763) for 1 hour at room temperature. Hybridization buffer (Empire Genomics Cat.
855 No. 16250) with or without HSat3 probe at 0.4 ng / µL was added to the samples,
856 followed by heat denaturation in an oven and overnight hybridization: 5 minutes 83C, 5
857 minutes 37C, 10 minutes 83C, and 37 C overnight in a humid chamber. Samples were
858 then washed three times for 5 minutes in 2x SSC at 37 C, and three times in 0.1x SSC
859 at room temperature. Finally, nuclei were stained with DAPI at 1 µg / mL for 10 minutes
860 at room temperature, followed by a PBS rinse. Control samples showed loss of
861 mScarlet fluorescence after FISH treatment, and strong signal for HSat3 without
862 immunofluorescence staining of ZFsat3-mScarlet.
863
864 The HSat3 probe sequence is: “ATT+ CCA+ TTC+ CAT+ TCC+ ATT+ CC”, where “+”
865 bases are linked nucleic acids. The probe was labeled with Alexa 594 at the 5’ end, and
866 purified by HPLC (Integrated DNA Technologies, custom order).
867
868 **HSat3 colocalization assay:**
869 The imaging screen of HSat3 binding factors was carried out by transient transfection in
870 293T cells in 96-well imaging plates with 400uL of media per cell (Ibidi Cat.No:89626**).**
871 The day before transfection 30k cells were plated per well. On the day of transfection,

872 each well was transfected using Lipofectamine 3000 (Thermo Fisher Cat L3000001)
873 following the manufacturer's protocol. For single color imaging, 200 ng of the HSat3 TF
874 was transfected. For two-color colocalization, 60ng ZFsat3-megfp and 180 ng of the
875 HSat3 TF was transfected. 8 hrs post transfection, cell media was washed once.
876
877 **DiMeLo-seq:**
878 Samples were prepared following the v2 protocol
879 (dx.doi.org/10.17504/protocols.io.b2u8qezw) with the following modifications: Reagents
880 for the following experiment were freshly prepared, syringe filtered through a 0.2-µm
881 filter, and then placed on ice. Cells were grown in 75 cm2 flasks at 37ºC in 5% CO2,
882 with 4 million live cells used per sample. Cells were pelleted at 500g for 3 minutes at
883 4ºC and washed with PBS. To isolate nuclei, cells were resuspended in 1 mL of Dig-
884 Wash Buffer (0.02% digitonin, 20 mM HEPES-potassium hydroxide buffer, pH 7.5,
885 150 mM sodium chloride, 0.5 mM spermidine, 1 Roche cOmplete EDTA-free tablet
886 (11873580001) per 50 ml buffer and 0.1% BSA) and incubated on ice for 5 minutes and
887 subsequently spun down at 500g for 3 minutes at 4ºC. All consecutive spins were
888 performed with the same conditions using wide bore tips for pipetting. The nuclei pellet
889 was resolved in 75 µl of Tween-Wash Buffer (0.1% Tween-20, 20 mM HEPES-
890 potassium hydroxide, pH 7.5, 150 mM sodium chloride, 0.5 mM spermidine, 1 Roche
891 cOmplete EDTA-free tablet per 50 ml buffer and 0.1% BSA) containing primary antibody
892 at a 1:50 dilution and then placed on a rotator at 4ºC overnight. For exogenous
893 expression of TEAD1-mscarlet in 293T cells, we used anti-RFP primary antibody
894 (Rockland Immunochemicals, Cat. No. 600-401-379). For endogenous TEAD1 in
895 MCF10A, we used anti-TEAD1 rabbit (CST Cat. No. 12292S).
896
897 Genomic DNA was extracted using NEB Monarch gDNA Extraction Kit (NEB Cat no
898 T3010S). 1.5 µg of purified DNA from each sample was input into library preparation
899 using the Native Barcoding Kit 24 V14 (Oxford Nanopore Technologies cat. no. SQK-
900 NBD114.24). The library preparation was carried out according to the manufacturer's
901 protocol, with the following modifications: End-repair incubation time was increased to
902 10 minutes. A total of 221.5 ng of end-repaired DNA was loaded into the barcode
903 ligation. LFB was used for the final adapter ligation clean up. Then, approximately 38.4
904 fmoles of the final pooled library was loaded onto the sequencer.
905
906 Sequencing was performed on a PromethION 2 Solo for 2-3 days using R10.4.1 flow
907 cells.
908
909 All Pod5 files generated during sequencing were merged into a single Pod5 file using
910 the pod5 merge command from the Pod5 package. Following this, Read IDs were
911 extracted from the merged file using the pod5 view command. Once the Read IDs were

obtained, alignment to the CHM13v2.0 genome was conducted. This process included DNA base calling, base modification calling, and demultiplexing utilizing dorado version 0.7.2 Linux x64. The resulting alignments were further merged, filtered, and indexed using samtools.

DiMeLo-seq analysis:

For analyzing m6A deposition centered at known binding sites, fibertools center was used to extract m6A base modifications centered at known ChIP-seq peaks defined by a bed file. Then reference matched base modifications were summed over a defined window centered at either ChIP-peaks or defined TF binding motifs within chip-peaks.

Known TF binding sites were collected from existing ChIP-seq data (listed below). Published narrowpeak files were first lifted over to the T2T-CHM13v2.0 (HS1) assembly using UCSC hgLiftOver (https://genome.ucsc.edu/cgi-bin/hgLiftOver). The resulting bed file was used to center ONT reads and quantify m6A modifications.

Chip-peak sources:
TEAD4: GSE66081
FOXA1: ENCODE (narrowPeak: ENCFF942VEL)

For quantifying deposition of m6A in satellite DNA, reads aligning to specified satellite regions were extracted using samtools view, then fibertools extract was used to identify modified bases on each read. We used a read length minimum of 2,000 bases, minimum mean base quality of 20 per read, and m6A minimum score 225 out 255.

Metaphase spreads:

Immunofluorescence of TEAD1-eGFP on metaphase nuclei using GFP-booster 488 (Chromotek Cat. No. gb2AF488) was performed following the protocol in Terrenoire et al[74] with modifications. MCF10A TEAD1-eGFP knock-in cells were treated with 0.1 ug/mL colcemid overnight (~15 hrs) to enrich mitotic nuclei. Cells were collected by trypsinization, resuspending in media, and spinning cells at 300g for 5 minutes. The cell pellet was resuspended in ice cold 75mM KCl at 4E5 cells/mL for 10 minutes on ice. After gently resuspending, cells were spun on a Shandon Cytospin 2 centrifuge, loaded at 200uL per funnel, at 1800 rpm for 10 minutes. Slides were then incubated in KCM buffer (120 mM KCl, 20 mM NaCl, 10 mM Tris/HCl pH 8.0, 0.5 mM EDTA, 0.1% Triton X-100) for 10 minutes at room temperature. Slides were incubated with GFP-booster 488 diluted 1:1000 in 3% BSA for 2 hours at room temperature, rinsed 3 times in PBS using, and mounted using Vectashield with DAPI (Vector Laboratories Cat. No. H-1200-10). Slides were imaged using 100X objective on a Delta Vision fluorescence microscope, followed by 3D deconvolution using default settings.

952 **Imaging of YAP-truncations:**
953 A Zeiss 980 Airyscan 2 was used to perform live-cell super-resolution imaging of
954 various YAP-truncations stably expressed MCF10A cells. Lentiviruses were packaged
955 as described above, and were used to tranduce WT MCF10A cells. Stable expression
956 was achieved using puromycin at 1ug/mL. 40,000 cells were seeded on Mattek #1.5
957 imaging dishes (Mattek Cat. No. P35G-1.5-10-C) overnight. Prior to imaging, cell nuclei
958 were stained with Sir-DNA for 1 hr at 1 μM, followed by a 5 min wash in warm media.
959
960 Samples were imaged live in an incubation unit at 37 C and 5% CO2. Two color
961 imaging was performed, followed by 3D Airyscan image processing using default
962 settings in Zeiss Zen software. Image segmentation is described below in "Microscopy
963 segmentation and quantification".
964
965 **Transcription reporter constructs**
966 The RNA Pol-I reporter was inspired by Ghoshal et al[75]. The promoter, including the
967 upstream binding enhancer and TTF1 binding sites through to the transcription start site
968 was cloned into a PUC19 backbone, followed by an IRES, mEGFP, polyA, and
969 downstream TTF1 sites to drive termination of Pol-I. Separately, a 2X copy of the pW1
970 HSat3 amplicon was cloned using restriction sites. The 2xpW1 (180Xbp) or an 1800bp
971 region from the PAWR human gene was then inserted directly ahead of the Pol-I
972 promoter.
973
974 The reporters were co-transfected with a control 2xNLS-mScarlet construct, or
975 transgene known to bind HSat3. All co-transfected constructs were cloned into pHIV
976 backbone driven by an EF1 promoter. To simply co-expression of a single activator, a
977 TEAD1-YAP chimera was generated as follows from N to C-terminus: DNA-binding
978 domain of TEAD1, linker, mScarlet, NLS, linker, and the C-terminus of YAP containing
979 the transcription activation domain (TAD) or VP64 subcloned from Addgene plasmid #
980 61422. The 2xNLS control construct was generated by NEB HiFi assembly, with primers
981 that encode the NLS's. The ZFsat3-YAP(TAD) construct was generated by truncating
982 full length YAP to just the WW+TAD domains.
983
984 **Transcription reporter assays**
985 The activity from the RNA Pol-I reporters were assayed using transient transfection of
986 293T cells using Lipofectamine 3000 (Thermo Fisher Cat L3000001). 80,000 293T cells
987 were seeded
988 on 24-well Ibidi imaging plates (Ibidi Cat. No. 82426) overnight. The following day, cells
989 were transfected with 300 ng of the reporter construct and 200 ng TEAD-YAP, ZFsat3-
990 YAP, TEAD-VP64, ZFsat3-KRAB-MECP2, or 60 ng of 2xNLS-mScarlet in optimem.

991 After 6 hours, transfection reagent was removed, and replaced with cell culture media.
992 Cells were imaged 24 hours after the start of transfection.
993
994 The specificity of this construct was tested using the RNA Pol-I inhibitors actinomycin-D
995 at 50ng/μL and BMH-21 at 2 μM. Inhibitors were added after the initial 6 hour
996 transfection period.
997
998 **CRISPR knock-in cell lines**
999 CRISPR knock-in cell lines were generated using previously described methods[44]. In
1000 this work, the YAP-degron homologous recombination plasmid was generated by
1001 cloning the FKBP12 mutant domain into the YAP-eGFP-p2a-puro plasmid. For
1002 MCF10A, we used Viafect (Promega Cat. No. E4981), with a 8 μL reagent to 2 μg
1003 plasmid DNA (1.33 μg HR backbone, 0.67 μg px459 vector with YAP-KI sgRNA). H1
1004 hESCs, we used Lipofectamine Stem Reagent (ThermoFisher Cat. No. STEM00003)
1005 with 5 μL reagent to 2.5 μg plasmid DNA (1.67 μg HR backbone, 0.83 μg px459 vector
1006 with YAP-KI sgRNA).
1007
1008 Cells were diluted and plated into a 96-well plate under puromycin selection for
1009 generating clonal cell lines. For H1 hESCs, we used 0.3 μg/mL puromycin selection, as
1010 cells were very sensitive to puromycin. We selected colonies with normal ESC
1011 morphology to assess the YAP-degron genotype using genomic PCRs and western blot
1012 (Supplementary Figure 21).
1013
1014 **Western blots**
1015 To confirm YAP-degron knock-in and rapid degradation, H1 YAP-degron clonal cells
1016 were seeded in 12-well tissue culture plates overnight following a 1:5 split ratio. Cultures
1017 were treated with DMSO, or 2 μM dTAG^{v}-1 for 15 and 30 minutes in the tissue culture
1018 incubator. Samples were lysed in the plate using Laemmli SDS buffer (ThermoFisher
1019 Cat. No. J61337.AD) supplemented with 5% β-mercaptoethanol, and boiled for 5
1020 minutes in a heat-block. Samples were run on a 4-12% Bis-Tris gel (Invitrogen Cat. No.
1021 NW04125BOX), with wet-transfer performed on a PVDF membrane. A 1 hour room
1022 temperature blocking was done with 2% Amersham ECL Prime Blocking Reagent
1023 (Cytiva Cat. No. RPN418) in Tris-buffered saline with 0.1% Tween 20. Membrane was
1024 cut to probe GAPDH (CST 2118S, 1:1000 dilution) and YAP (Santa Cruz sc-101199,
1025 1:1000 dilution) in 2% ECL Prime in TBST overnight, followed by 3x5 minute washes in
1026 TBST. Rabbit/mouse conjugated secondary antibodies were incubated on membranes
1027 in 2% ECL Prime in TBST for 1 hour, followed by 3x5 minute washes in TBST. The
1028 membrane was imaged using a Gel-doc? Imager following incubation with
1029 Westernbright Quantum HRP substrate (Advansta Cat. No. K-12042-C20).
1030

1031 **EU assays**
1032 To drive targeted repression of HSat3, we fused ZFsat3-mScarlet to KRAB-MECP2[61]
1033 sourced from dCas9-KRAB-MeCP2, a gift from Alejandro Chavez & George Church
1034 (Addgene plasmid # 110821 ; http://n2t.net/addgene:110821 ; RRID:Addgene_110821).
1035 As a negative control, we cloned a non-targeting construct mScarlet-KRAB-MECP2.
1036 Plasmids were assembled using restriction cloning (PCR primers in supplementary
1037 data, provided after publication).
1038
1039 Cells were seeded on 96-well imaging plates (Ibidi Cat.No:89626**)** at various densities to
1040 achieve 30-50% confluency on day of EU incorporation assay. For stable lentivirus
1041 transduced MCF10A lines (ZFsat3-mScarlet, ZFsat3-mScarlet-KRAB-MECP2,
1042 mScarlet), cells were seeded at 30k cells / cm^2, and assayed 48 hrs post seeding. For
1043 YAP-degron time series, H1 hESCs and MCF10A, cells were plated at 30k cells / cm^2,
1044 and assayed 48 hrs post seeding. For short term lentivirus transduction, cells were
1045 plated at 20k cells / cm2, transduced with lentivirus next morning, and assayed 72 hrs
1046 post seeding. All cultures were grown in 300 µL media. For H1 hESCs, wells were
1047 coated with 300 µL of Matrigel coating solution (see hESC cell culture methods) for at
1048 least 2 hrs at 37 °C in tissue culture incubator, followed by seeding cells in 300 µL
1049 mTESR Plus media. Media was changed daily for hESCs.
1050
1051 For YAP-degron experiments, dTAGv1 (Tocris Cat. No. 6914) or DMSO control was
1052 added at 2 µM for various times (15, 30, 60min) in fresh media, followed immediately by
1053 EU incorporation.
1054
1055 EU incorporation assay in all conditions was performed by addition of 1 mM 5-
1056 Ethynyluridine (Fisher Scientific 50-238-7038) directly to wells, and incubated for 1 hr in
1057 tissue culture incubator. Following incorporation, samples were gently washed twice in
1058 PBS, fixed with 4% paraformaldehyde for 10 minutes at room temperature, washed 2 X
1059 5 minutes in PBS, permeabilized for 5 minutes in 0.5% Triton X-100 in PBS, and
1060 washed 2 x 5 minutes in PBS.
1061
1062 The EU labeling reaction was carried out following the protocol in Jao & Salic [10]. The
1063 labeling reaction buffer was made fresh from 100 mM Tris pH 8.0, 1 mM CuSO4, µM
1064 iFluor 488 Azide (AAT Bioquest Cat. No. 1000), and 100 mM ascorbic acid added last
1065 from 500 mM stock in water. 300 µL of reaction buffer was then added to 96-wells for 90
1066 minutes at room temperature in the dark. 3 x 10 minute PBS washes were performed to
1067 thoroughly destain the unreacted azide dye. Cell nuclei were detected with DAPI (AAT
1068 Bioquest Cat. No. 17507) staining at 1 µM for 15 minutes.
1069
1070

1071 **Microscopy segmentation and quantification**
1072 3D segmentation of cell nuclei, nucleoli, and sub-nuclear HSat3 foci was performed
1073 using custom image segmentation software (https://github.com/jmfrank/track_analyzer).
1074
1075 *Nuclear segmentation*
1076 A 9X9X3 pixel median filter was performed, followed by intensity thresholding, hole-
1077 filling, watershedding, and object size filtering to identify distinct nuclei (all operations
1078 performed in 3D).
1079 *Nucleoli segmentation*
1080 The nucleoli were segmented by first using the nuclear segmentations as a positive
1081 mask, followed by a 3X3X1 median filter and a local intensity thresholding scheme.
1082 Nucleoli size and EU intensity is too variable between individual cells. Thus, the
1083 intensity threshold was determined on a per-cell basis. The nucleoli intensity threshold
1084 was set at 6 signal-to-noise ratio using the non-nucleolar pixels which empirically are
1085 the 10-60 intensity percentiles per cell nucleus. Object sizes are then filtered to obtain
1086 nucleoli masks. The nucleoli masks were used to measure mean intensity per nucleolus
1087 after subtracting a local background per nucleolus which is a 3D shell mask of width 2
1088 pixels starting at 6 pixels from the nucleolus boundary (ignoring pixels from other
1089 nucleoli in the same nucleus).
1090 *Colocalization:*
1091 ZFsat3-megfp foci were first segmented to provide a HSat3 reference location in cell
1092 nuclei. This segmented ROI was then used to analyze intensity of TF-mscarlet in a
1093 second channel. Because HSat3 arrays are variable in size, we first generated scatter
1094 plots to correlate signal intensities. Second, we generated 1D intensity profiles for the
1095 two channels by mapping 2D intensity to polar coordinates centered at the foci centroid
1096 position. This showed strong correlation for most top HSat3 candidates. However,
1097 SOX1 and NKX2-2 only showed colocalization for a small set of foci, so 1D line-profiles
1098 were generated manually using Fiji.
1099
1100 Image processing scripts provided upon request.
1101
1102 **Total RNA / DNA ratio in TEAD knock-out cells:**
1103 To estimate the impact of TEAD1-4 knock-out on total RNA expression, we estimated
1104 the total RNA to total DNA for cultures of MCF7 and MCF7 TEAD1-4 knockout (TEAD-
1105 qKO)[60]. Approximately 200,000-400,000 cells were collected in triplicate for each cell
1106 line using TrypLE Express. Cultures were split into equal volume and total RNA
1107 (Qiagen RNeasy Plus Universal Mini Kit Cat no. 73404) and total DNA (Qiagen Blood &
1108 Cell Culture DNA Mini Kit Cat no. 13323) were measured.
1109
1110

DATA AVAILABILITY

Raw data from DiMeLo-seq and microscopy experiments are available upon request and will be deposited in permanent repositories prior to publication. The library of mScarlet-tagged TFs will be deposited in Addgene prior to publication.

CODE AVAILABILITY

Custom scripts for performing data analysis for the TF motif and ChIP-seq screens will be made publicly available on github and in permanent repositories upon publication.

REFERENCES

1. Altemose, N. A classical revival: Human satellite DNAs enter the genomics era. *Seminars in Cell & Developmental Biology* **128**, 2–14 (2022) PMID: 35487859.

2. Shestakova, E. A., Mansuroglu, Z., Mokrani, H., Ghinea, N. & Bonnefoy, E. Transcription factor YY1 associates with pericentromeric gamma-satellite DNA in cycling but not in quiescent (G0) cells. *Nucleic Acids Res.* **32**, 4390–4399 (2004) PMID: 15316102.

3. Jolly, C. *et al.* Stress-induced transcription of satellite III repeats. *Journal of Cell Biology* **164**, 25–33 (2004) PMID: 14699086.

4. Shadle, S. C. *et al.* DUX4-induced bidirectional HSATII satellite repeat transcripts form intranuclear double-stranded RNA foci in human cell models of FSHD. *Human Molecular Genetics* **28**, 3997–4011 (2019) PMID: 31630170.

5. Kim, J. H. *et al.* Human gamma-satellite DNA maintains open chromatin structure and protects a transgene from epigenetic silencing. *Genome Research* **19**, 533 (2009) PMID: 19141594.

6. Ruzanov, P. *et al.* Oncogenic ETS fusions promote DNA damage and proinflammatory responses via pericentromeric RNAs in extracellular vesicles. *J. Clin. Invest.* **134**, (2024) PMID: 38530366.

7. Shatskikh, A. S., Kotov, A. A., Adashev, V. E., Bazylev, S. S. & Olenina, L. V. Functional significance of satellite DNAs: Insights from Drosophila. *Front. Cell Dev. Biol.* **8**, 312 (2020) PMID: 32432114.

8. Nurk, S. *et al.* The complete sequence of a human genome. *Science* **376**, 44–53 (2022) PMID: 35357919.

9. Yoo, D. *et al.* Complete sequencing of ape genomes. *bioRxivorg* 2024.07.31.605654 (2024) PMID: 39131277.

10. Altemose, N. *et al.* Complete genomic and epigenetic maps of human centromeres. *Science* **376**, (2022) PMID: 35357911.

11. Corless, S. *et al.* The bromodomain inhibitor JQ1 is a molecular glue targeting centromeres. *bioRxiv* 2023.03.15.532673 (2023) doi:10.1101/2023.03.15.532673.

12. Yasmineh, W. G. & Yunis, J. J. Satellite DNA in mouse autosomal heterochromatin. *Biochem. Biophys. Res. Commun.* **35**, 779–782 (1969) PMID: 5791516.

13. Waldron, R. *et al.* JRK binds satellite III DNA and is necessary for the heat shock response. *Cell Biol. Int.* **48**, 1212–1222 (2024) PMID: 38946594.

14. Marshall, O. J. & Choo, K. H. A. Putative CENP-B paralogues are not present at mammalian centromeres. *Chromosoma* **121**, 169–179 (2012) PMID: 22080934.

15. Zheng, Y. & Pan, D. The Hippo Signaling Pathway in Development and Disease. *Dev. Cell* **50**, 264–282 (2019) PMID: 31386861.

16. Franklin, J. M., Wu, Z. & Guan, K. L. Insights into recent findings and clinical application of YAP and TAZ in cancer. *Nat. Rev. Cancer* **23**, 512–525 (2023) PMID: 37308716.

1164 17. Rauluseviciute, I. *et al.* JASPAR 2024: 20th anniversary of the open-access
1165 database of transcription factor binding profiles. *Nucleic Acids Res.* **52**, D174–D182
1166 (2024) PMID: 37962376.

1167 18. Altemose, N., Miga, K. H., Maggioni, M. & Willard, H. F. Genomic Characterization
1168 of Large Heterochromatic Gaps in the Human Genome Assembly. *PLOS Computational*
1169 *Biology* **10**, e1003628 (2014) PMID: 24831296.

1170 19. Prosser, J., Frommer, M., Paul, C. & Vincent, P. C. Sequence relationships of three
1171 human satellite DNAs. *J. Mol. Biol.* **187**, 145–155 (1986) PMID: 3701863.

1172 20. Jolly, C. *et al.* In vivo binding of active heat shock transcription factor 1 to human
1173 chromosome 9 heterochromatin during stress. *J. Cell Biol.* **156**, 775–781 (2002) PMID:
1174 11877455.

1175 21. Luo, Y. *et al.* New developments on the Encyclopedia of DNA Elements (ENCODE)
1176 data portal. *Nucleic Acids Res.* **48**, D882–D889 (2020) PMID: 31713622.

1177 22. Rhie, A. *et al.* The complete sequence of a human Y chromosome. *Nature* **621**,
1178 344–354 (2023) PMID: 37612512.

1179 23. Dastidar, S. G. *et al.* Transcriptional responses of cancer cells to heat shock-
1180 inducing stimuli involve amplification of robust HSF1 binding. *Nat. Commun.* **14**, 7420
1181 (2023) PMID: 37973875.

1182 24. Crabtree, G. R. & Olson, E. N. NFAT signaling: choreographing the social lives of
1183 cells. *Cell* **109 Suppl**, S67–79 (2002) PMID: 11983154.

1184 25. Ma, H. *et al.* Multicolor CRISPR labeling of chromosomal loci in human cells. *Proc.*
1185 *Natl. Acad. Sci. U. S. A.* **112**, 3002–3007 (2015) PMID: 25713381.

1186 26. Stein, C. *et al.* YAP1 Exerts Its Transcriptional Control via TEAD-Mediated
1187 Activation of Enhancers. *PLOS Genetics* **11**, e1005465 (2015).

1188 27. Thul, P. J. *et al.* A subcellular map of the human proteome. *Science* **356**, (2017)
1189 PMID: 28495876.

1190 28. Soderholm, J. F. *et al.* Importazole, a small molecule inhibitor of the transport
1191 receptor importin-β. *ACS Chem. Biol.* **6**, 700–708 (2011) PMID: 21469738.

1192 29. Lin, R., Heylbroeck, C., Pitha, P. M. & Hiscott, J. Virus-dependent phosphorylation
1193 of the IRF-3 transcription factor regulates nuclear translocation, transactivation
1194 potential, and proteasome-mediated degradation. *Mol. Cell. Biol.* **18**, 2986–2996 (1998)
1195 PMID: 9566918.

1196 30. Qin, Z. *et al.* Deactylation by SIRT1 enables liquid-liquid phase separation of
1197 IRF3/IRF7 in innate antiviral immunity. *Nat. Immunol.* **23**, 1193–1207 (2022) PMID:
1198 35879450.

1199 31. Yu, Y. *et al.* PRDM15 interacts with DNA-PK-Ku complex to promote
1200 radioresistance in rectal cancer by facilitating DNA damage repair. *Cell Death Dis.* **13**,
1201 1–13 (2022) PMID: 36402747.

1202 32. Mzoughi, S. *et al.* PRDM15 safeguards naive pluripotency by transcriptionally
1203 regulating WNT and MAPK-ERK signaling. *Nat. Genet.* **49**, 1354–1363 (2017) PMID:

1204 28740264.

1205 33. Mzoughi, S., Tan, Y. X., Low, D. & Guccione, E. The role of PRDMs in cancer: one
1206 family, two sides. *Curr. Opin. Genet. Dev.* **36**, 83–91 (2016) PMID: 27153352.

1207 34. Ma, R. *et al.* Targeting pericentric non-consecutive motifs for heterochromatin
1208 initiation. *Nature 2024* 1–8 (2024).

1209 35. Altemose, N. *et al.* DiMeLo-seq: a long-read, single-molecule method for mapping
1210 protein–DNA interactions genome wide. *Nature Methods 2022 19:6* **19**, 711–723 (2022)
1211 PMID: 35396487.

1212 36. Macian, F. NFAT proteins: key regulators of T-cell development and function. *Nat.*
1213 *Rev. Immunol.* **5**, 472–484 (2005) PMID: 15928679.

1214 37. Al Hamrashdi, M. & Brady, G. Regulation of IRF3 activation in human antiviral
1215 signaling pathways. *Biochem. Pharmacol.* **200**, 115026 (2022) PMID: 35367198.

1216 38. Ramdzan, Z. M. & Nepveu, A. CUX1, a haploinsufficient tumour suppressor gene
1217 overexpressed in advanced cancers. *Nat. Rev. Cancer* **14**, 673–682 (2014) PMID:
1218 25190083.

1219 39. Currey, L., Thor, S. & Piper, M. TEAD family transcription factors in development
1220 and disease. *Development* **148**, dev196675 (2021) PMID: 34128986.

1221 40. Marella, N. V. *et al.* Cytogenetic and cDNA microarray expression analysis of
1222 MCF10 human breast cancer progression cell lines. *Cancer Res.* **69**, 5946–5953 (2009)
1223 PMID: 19584277.

1224 41. Hao, S. *et al.* YAP condensates are highly organized hubs. *iScience* **27**, 109927
1225 (2024) PMID: 38784009.

1226 42. Zhang, H. *et al.* Reversible phase separation of HSF1 is required for an acute
1227 transcriptional response during heat shock. *Nat. Cell Biol.* **24**, 340–352 (2022) PMID:
1228 35256776.

1229 43. Zanconato, F. *et al.* Genome-wide association between YAP/TAZ/TEAD and AP-1
1230 at enhancers drives oncogenic growth. *Nat. Cell Biol.* **17**, 1218–1227 (2015) PMID:
1231 26258633.

1232 44. Franklin, J. M., Ghosh, R. P., Shi, Q., Reddick, M. P. & Liphardt, J. T. Concerted
1233 localization-resets precede YAP-dependent transcription. *Nat. Commun.* **11**, 1–18
1234 (2020) PMID: 32917893.

1235 45. Chen, Y.-A. *et al.* WW domain-containing proteins YAP and TAZ in the Hippo
1236 pathway as key regulators in stemness maintenance, tissue homeostasis, and
1237 tumorigenesis. *Front. Oncol.* **9**, 60 (2019) PMID: 30805310.

1238 46. Kaplan, F. S. *et al.* The topographic organization of repetitive DNA in the human
1239 nucleolus. *Genomics* **15**, 123–132 (1993) PMID: 8432523.

1240 47. Brändle, F., Frühbauer, B. & Jagannathan, M. Principles and functions of
1241 pericentromeric satellite DNA clustering into chromocenters. *Semin. Cell Dev. Biol.* **128**,
1242 26–39 (2022) PMID: 35144860.

1243 48. Efroni, S. *et al.* Global transcription in pluripotent embryonic stem cells. *Cell Stem*

1244 *Cell* **2**, 437–447 (2008) PMID: 18462694.

1245 49. Teves, S. S. *et al.* A dynamic mode of mitotic bookmarking by transcription factors.
1246 *Elife* **5**, (2016).

1247 50. Yu, Q. *et al.* Dynamics and regulation of mitotic chromatin accessibility
1248 bookmarking at single-cell resolution. *Sci. Adv.* **9**, eadd2175 (2023) PMID: 36696508.

1249 51. Woolnough, J. L., Atwood, B. L., Liu, Z., Zhao, R. & Giles, K. E. The Regulation of
1250 rRNA Gene Transcription during Directed Differentiation of Human Embryonic Stem
1251 Cells. *PLoS One* **11**, e0157276 (2016).

1252 52. Lu, Y. Phase separation of TAZ compartmentalizes the transcription machinery to
1253 promote gene expression. *Nature Cell Biology* (2020).

1254 53. Cai, D. *et al.* Phase separation of YAP reorganizes genome topology for long-term
1255 YAP target gene expression. *Nature Cell Biology* **21**, 1578–1589 (2019).

1256 54. Manning, S. A. *et al.* Dynamic Fluctuations in Subcellular Localization of the Hippo
1257 Pathway Effector Yorkie In Vivo. *Curr. Biol.* **28**, 1651–1660.e4 (2018) PMID: 29754899.

1258 55. Gu, B. *et al.* Live imaging YAP signalling in mouse embryo development. *Open Biol.*
1259 **12**, 210335 (2022) PMID: 35042406.

1260 56. Palazzo, A. F. & Lee, E. S. Non-coding RNA: what is functional and what is junk?
1261 *Front. Genet.* **6**, 2 (2015) PMID: 25674102.

1262 57. Jarmuz, M., Glotzbach, C. D., Bailey, K. A., Bandyopadhyay, R. & Shaffer, L. G.
1263 The evolution of satellite III DNA subfamilies among primates. *Am. J. Hum. Genet.* **80**,
1264 495–501 (2007) PMID: 17273970.

1265 58. Grandori, C. *et al.* c-Myc binds to human ribosomal DNA and stimulates
1266 transcription of rRNA genes by RNA polymerase I. *Nat. Cell Biol.* **7**, 311–318 (2005)
1267 PMID: 15723054.

1268 59. Antony, C. *et al.* Control of ribosomal RNA synthesis by hematopoietic transcription
1269 factors. *Molecular Cell* **82**, 3826–3839.e9 (2022) PMID: 36113481.

1270 60. Ma, S. *et al.* Transcriptional repression of estrogen receptor alpha by YAP reveals
1271 the Hippo pathway as therapeutic target for ER + breast cancer. *Nat. Commun.* **13**,
1272 (2022) PMID: 35217640.

1273 61. Yeo, N. C. *et al.* An enhanced CRISPR repressor for targeted mammalian gene
1274 regulation. *Nat. Methods* **15**, 611–616 (2018) PMID: 30013045.

1275 62. Jao, C. Y. & Salic, A. *Exploring RNA transcription and turnover in vivo by using click*
1276 *chemistry*. (2008).

1277 63. Allshire, R. C. & Madhani, H. D. Ten principles of heterochromatin formation and
1278 function. *Nat. Rev. Mol. Cell Biol.* **19**, 229–244 (2018) PMID: 29235574.

1279 64. Yasuhara, J. C. & Wakimoto, B. T. Oxymoron no more: the expanding world of
1280 heterochromatic genes. *Trends Genet.* **22**, 330–338 (2006) PMID: 16690158.

1281 65. Miklos, G. L. & John, B. Heterochromatin and satellite DNA in man: properties and
1282 prospects. *Am. J. Hum. Genet.* **31**, 264–280 (1979) PMID: 111544.

66. Tang, Y. *et al.* A cofactor-induced repressive type of transcription factor condensation can be induced by synthetic peptides to suppress tumorigenesis. *EMBO J.* **43**, 5586–5612 (2024) PMID: 39358623.

67. Plouffe, S. W. *et al.* The Hippo pathway effector proteins YAP and TAZ have both distinct and overlapping functions in the cell. *J. Biol. Chem.* **293**, 11230–11240 (2018).

68. Reggiani, F., Gobbi, G., Ciarrocchi, A. & Sancisi, V. YAP and TAZ are not identical twins. *Trends Biochem. Sci.* **46**, 154–168 (2021) PMID: 32981815.

69. Smirnov, E., Chmúrčiaková, N. & Cmarko, D. Human rDNA and cancer. *Cells* **10**, 3452 (2021) PMID: 34943960.

70. Judson, R. N. *et al.* The Hippo pathway member Yap plays a key role in influencing fate decisions in muscle satellite cells. *J. Cell Sci.* **125**, 6009–6019 (2012) PMID: 23038772.

71. Hwang, D. *et al.* YAP promotes global mRNA translation to fuel oncogenic growth despite starvation. *Exp. Mol. Med.* 1–14 (2024) PMID: 39349825.

72. Li, H. Aligning sequence reads, clone sequences and assembly contigs with BWA-MEM. *arXiv [q-bio.GN]* (2013).

73. Wright, D. A. *et al.* Standardized reagents and protocols for engineering zinc finger nucleases by modular assembly. *Nat. Protoc.* **1**, 1637–1652 (2006) PMID: 17406455.

74. Terrenoire, E. *et al.* Immunostaining of modified histones defines high-level features of the human metaphase epigenome. *Genome Biol.* **11**, R110 (2010) PMID: 21078160.

75. Ghoshal, K. *et al.* Role of Human Ribosomal RNA (rRNA) Promoter Methylation and of Methyl-CpG-binding Protein MBD2 in the Suppression of rRNA Gene Expression*. *Journal of Biological Chemistry* **279**, 6783–6793 (2003).

ACKNOWLEDGEMENTS

We thank Nathan Gamarra for the many fruitful discussions for analyzing and interpreting data, as well as Sylvia Erhardt and Samuel Corless for useful discussions regarding ChIP-seq analysis. *Core facilities:* Stowers Institute Microscopy Core, Stanford University Cell Sciences Imaging Core Facility (RRID:SCR_017787). Figure 3a was created in BioRender, https://BioRender.com/s4wcmqh.

FUNDING

JMF was supported by a NIH T32 Fellowship (NIH/NCI T32 CA009523) and a Stanford Community of Shared Research Platforms – C-ShaRP Grant (RRID:SCR_022986). NA is a Pew Biomedical Scholar, an HHMI Hanna Gray Faculty Fellow, and a Chan Zuckerberg Biohub – San Francisco Investigator.

CONTRIBUTIONS

JMF conceived the project. JMF, DD, NA, KLG, JLG designed the computational and experimental strategies. JMF performed the motif search and analysis. DD performed the ENCODE ChIP-seq analysis. JMF generated TF fusion constructs, microscopy data, stable expression cell lines, gene edits, and western blots. JMF performed image quantification. CC, AB, RJL, JMF performed DiMeLo-seq, ONT sequencing, and basecalling. JMF performed DiMeLo-seq analysis. RPG designed CRISPR knock-in strategy. JMF and NA wrote and edited the manuscript. JMF and NA generated figures. KLG, NA, and JLG provided project funding and supervision.

COMPETING INTERESTS

JMF is an inventor on a patent application related to the work presented in this manuscript.

1338 **SUPPLEMENTARY FIGURES**

1339

1340

1341 **Supplementary Figure 1:** Distribution of HSat3 array sizes in T2T-CHM13v2.0.

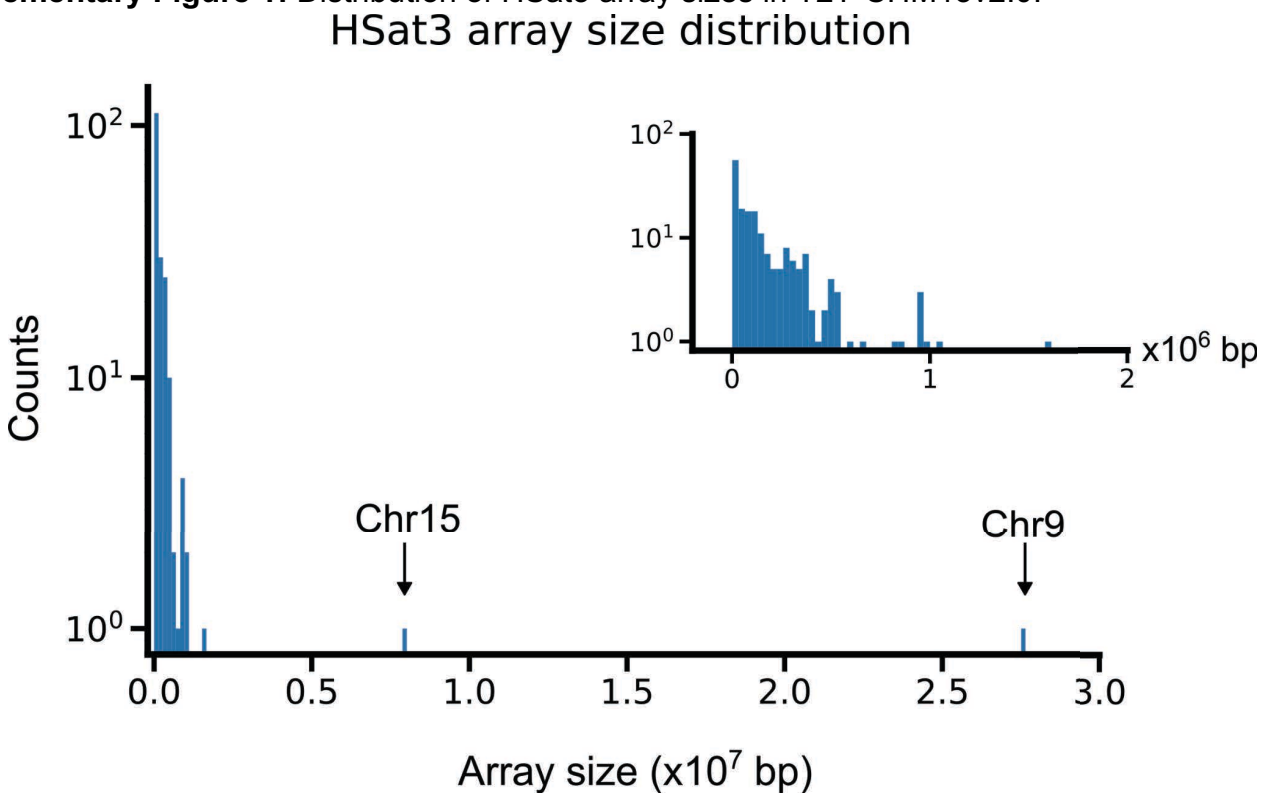

1342

1343 **Supplementary Figure 2:** Ranked HSat3 motifs for all sub-families.

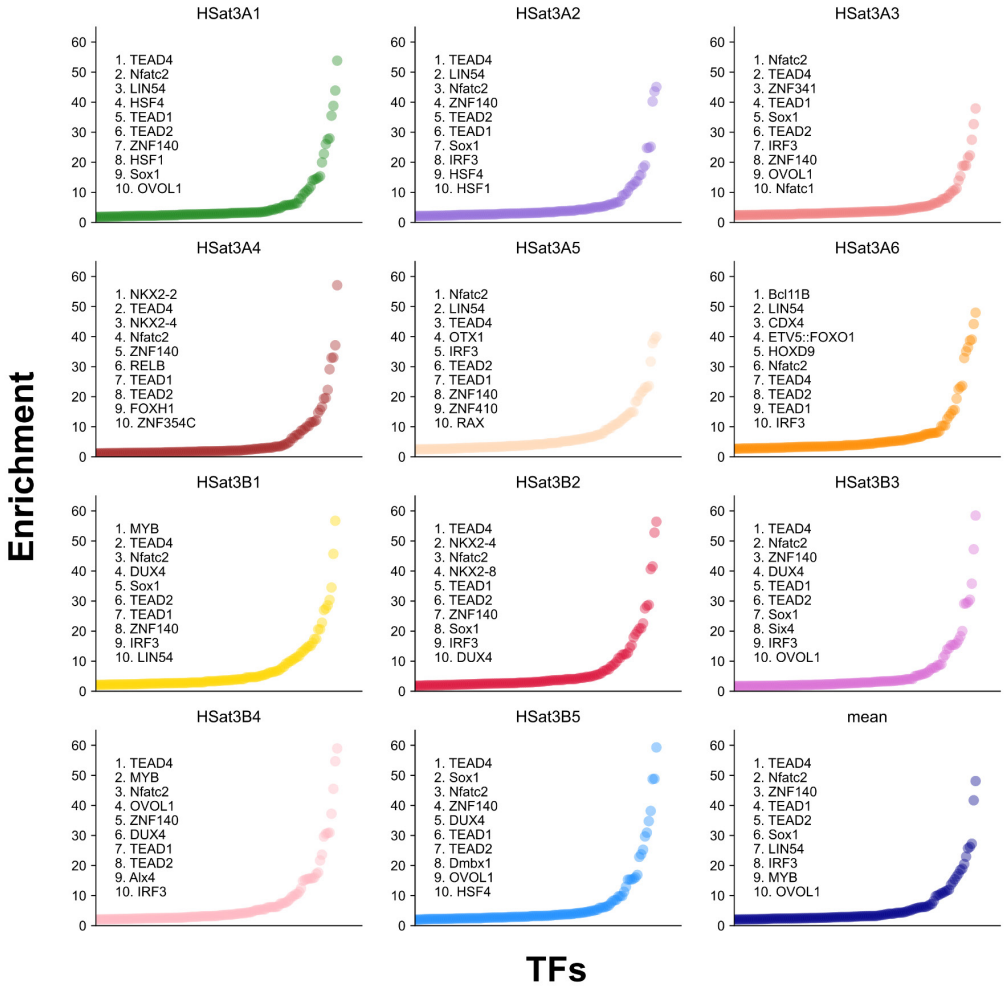

1344

1345 **Supplementary Figure 3:** ETS-family motifs in HSat3

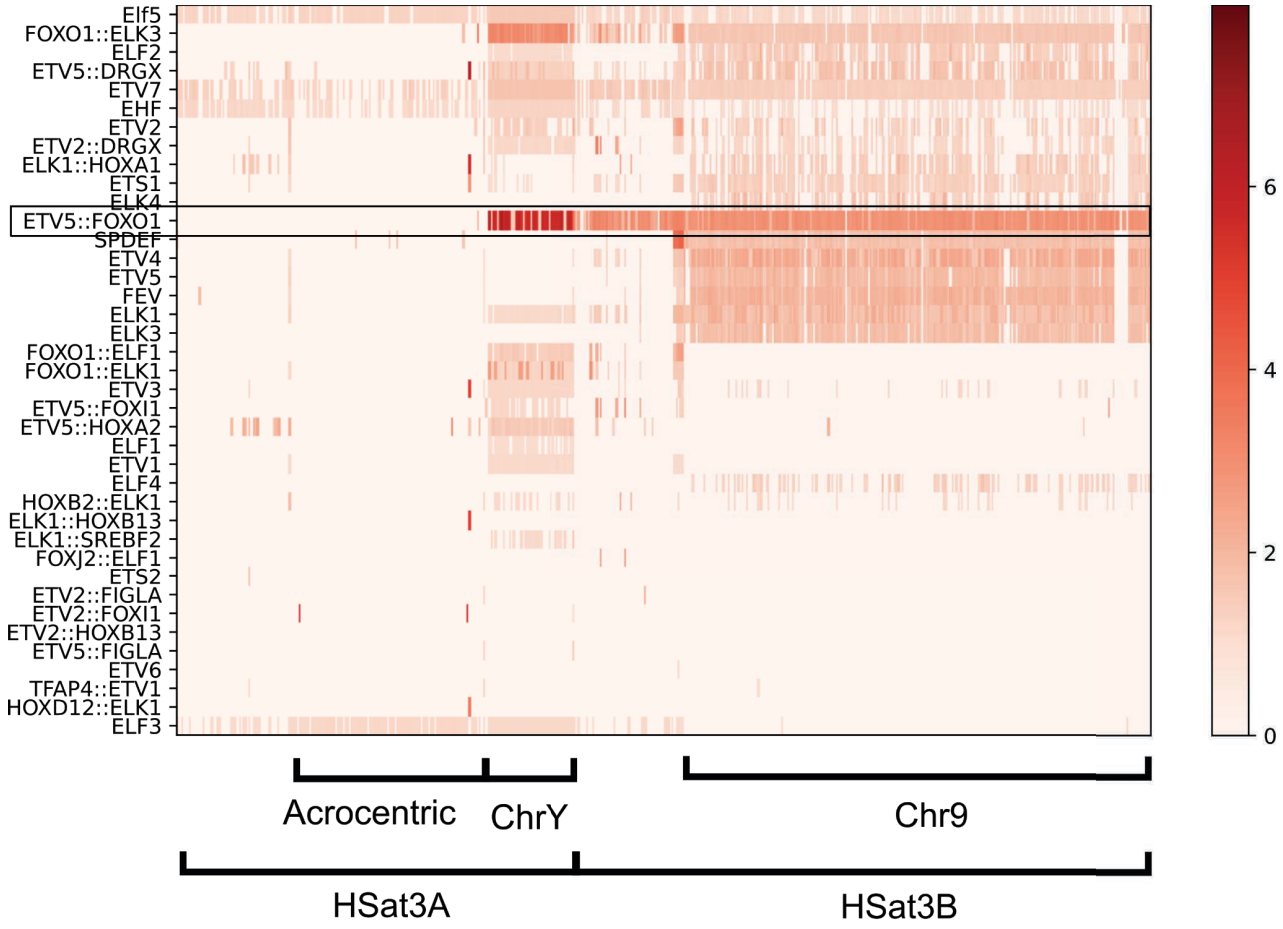

1346

1347 **Supplementary Figure 4:** Estimation of TEAD family motifs within HSat3
1348

Motif	Motifs in CHM13v2.0	Motifs in HSat3 arrays	Percent
TEAD1 (MA0090.4)	869867	255391	29%
TEAD2 (MA1121.2)	688308	167910	24%
TEAD3 (MA0808.1)	294882	124048	42%
TEAD4 (MA0809.3)	721924	416061	58%
CATTCC/GGAATG	6790676	4868988	72%

1349
1350 TEAD motif counts, and percentage of TEAD motifs in HSat3 arrays in
1351 CHM13v2.0. TEAD1-4 motifs were obtained from JASPAR[17]**.** The same metrics
1352 are reported for the core 6 bases present in all TEAD motifs (GGAATG) as a
1353 theoretical maximum for TEAD binding sites.

Supplementary Figure 5: Top 10 HSat3-enriched factors per cell line using ENCODE ChIP-seq data from 13 cell lines. Columns are pairs of cell line followed by the enrichment score. Note, not all factors are tested in all cell lines. Full dataset can be found in supplementary data.

K562	K562_e	HEK293	HEK293_e	GM12878	GM12878_e	MCF-7	MCF-7_e	HEK293T	HEK293T_e	SK-N-SH	SK-N-SH_e
CTCFL	2.614275	ZNF311	2.904626	FOXK2	6.813107	E4F1	3.504806	BHLHE40	2.001958	RARB	1.464218
CREBBP	2.577474	ZNF571	2.736061	IRF5	4.136432	MLLT1	3.197933	FOXK2	1.932941	PATZ1	1.375296
TAF9B	2.557403	ZNF521	2.644412	E4F1	3.641356	HSF1_HS	3.117097	SUZ12	1.913954	GLIS3	1.285969
COPS2	2.545667	ZNF621	2.535638	IKZF2	3.181927	FOXK2	2.785043	NFRKB	1.829507	TOX	1.257628
IKZF1	2.307223	ZSCAN26	2.471263	IKZF1	3.050927	CTBP1	2.701063	SP1	1.798790	ZBTB33	1.222312
TCF12	2.299068	ZNF544	2.459462	ZNF274	2.655356	ZBTB33	2.470153	L3MBTL2	1.724584	TCF4	1.222017
BCLAF1	2.272891	ZNF148	2.456139	ZZZ3	2.404381	HES1	2.465816	CTBP1	1.715824	SNAI2	1.214033
MCM5	2.125209	ZNF473	2.379923	FOS	2.355329	MTA2	2.330482	ELF4	1.589300	ZFP3	1.208767
MEF2A	2.102264	ZNF114	2.338412	CBX5	1.999043	ZKSCAN1	2.325522	ZNF384	1.477438	POU6F1	1.203152
MCM3	2.080229	ZNF248	2.247486	NR2C2	1.987856	NEUROD1	2.261944	PKNOX1	1.356504	ARNTL	1.156299

IMR-90	IMR-90_e	HepG2	HepG2_e	WTC11	WTC11_e	H1	H1_e	HCT116	HCT116_e	A549	A549_e	GM23338	GM23338_e
RCOR1	1.005230	JUNB	7.488320	ATF6	2.977312	CBX5	4.014691	ZNF274	4.588935	HMGXB4	1.605839	ZNF114	1.471728
ELK1	0.988678	PIN1	4.639362	NFE2L1	2.738289	MYC	2.720889	TEAD4	3.588758	TP53	1.594041	ZNF331	1.398599
RFX5	0.941643	HOXA7	4.395157	JUN	2.326801	RNF2	1.690392	REST	2.358449	NR2E3	1.480355	CREB1	1.212108
USF2	0.935280	PRDM15	4.344091	E2F4	2.322660	USF2	1.151916	TCF7L2	2.180738	ATOH8	1.271386	JUNB	1.071525
NFE2L2	0.916405	SKIL	4.183202	NR1H2	2.315310	ZNF143	1.141085	ATF3	2.096018	HES2	1.189227	STAT1	1.070744
FOS	0.899230	ZNF780A	4.043124	TCF7	2.040139	SAP30	1.136616	CEBPB	1.717331	ZNF302	1.187601	ETS1	0.994384
BHLHE40	0.888540	ZNF496	3.971537	FOXJ3	1.935403	BRCA1	1.121683	CBX3	1.703535	RARB	1.187349	POU5F1	0.967238
CHD1	0.881882	HOXA9	3.839361	ZNF512	1.909318	RFX5	1.040781	USF1	1.675420	FOXS1	1.169179	REST	0.943246
MAZ	0.841464	CSRNP2	3.830892	TEAD4	1.771173	CREB1	1.011739	SRF	1.573218	FOSB	1.144997	NANOG	0.921562
MXI1	0.824913	GRHL1	3.810991	ZNF219	1.766057	MXI1	1.006420	SIN3A	1.538590	EP300	1.127847	ZNF462	0.919345

Supplementary Figure 6: Correlation between ChIP-seq and motif enrichment analysis. Data points are colored by the HSat3 subfamily, and represent the mean value of a given factor's enrichment in ChIP-seq and motif analysis, for each cell line. The dashed line represents an enrichment cut-off threshold generated by HSF1 data in heat-shocked MCF7 cells (Figure 2b-c).

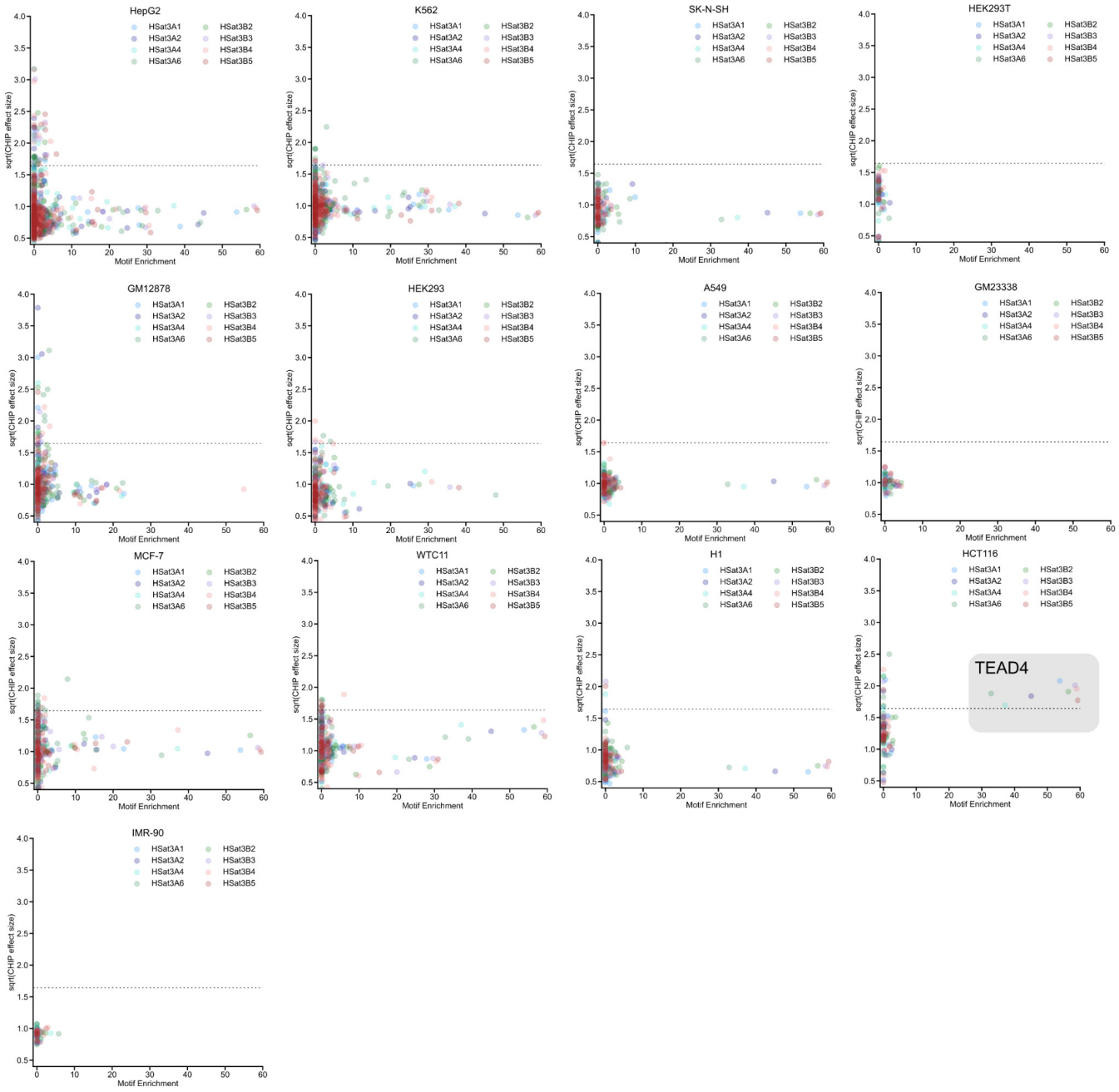

1367 **Supplementary Figure 7:** Immuno-FISH Validation of ZFsat3-mScarlet using HSat3-
1368 FISH. MCF10A cells stably expressing ZFsat3-mScarlet were prepared for immuno-
1369 FISH with 488-labeled anti-RFP, Alexa594-labeled HSat3 oligos with two control
1370 samples: (1) HSat3 FISH only and (2) neither anti-RFP or HSat3 FISH.

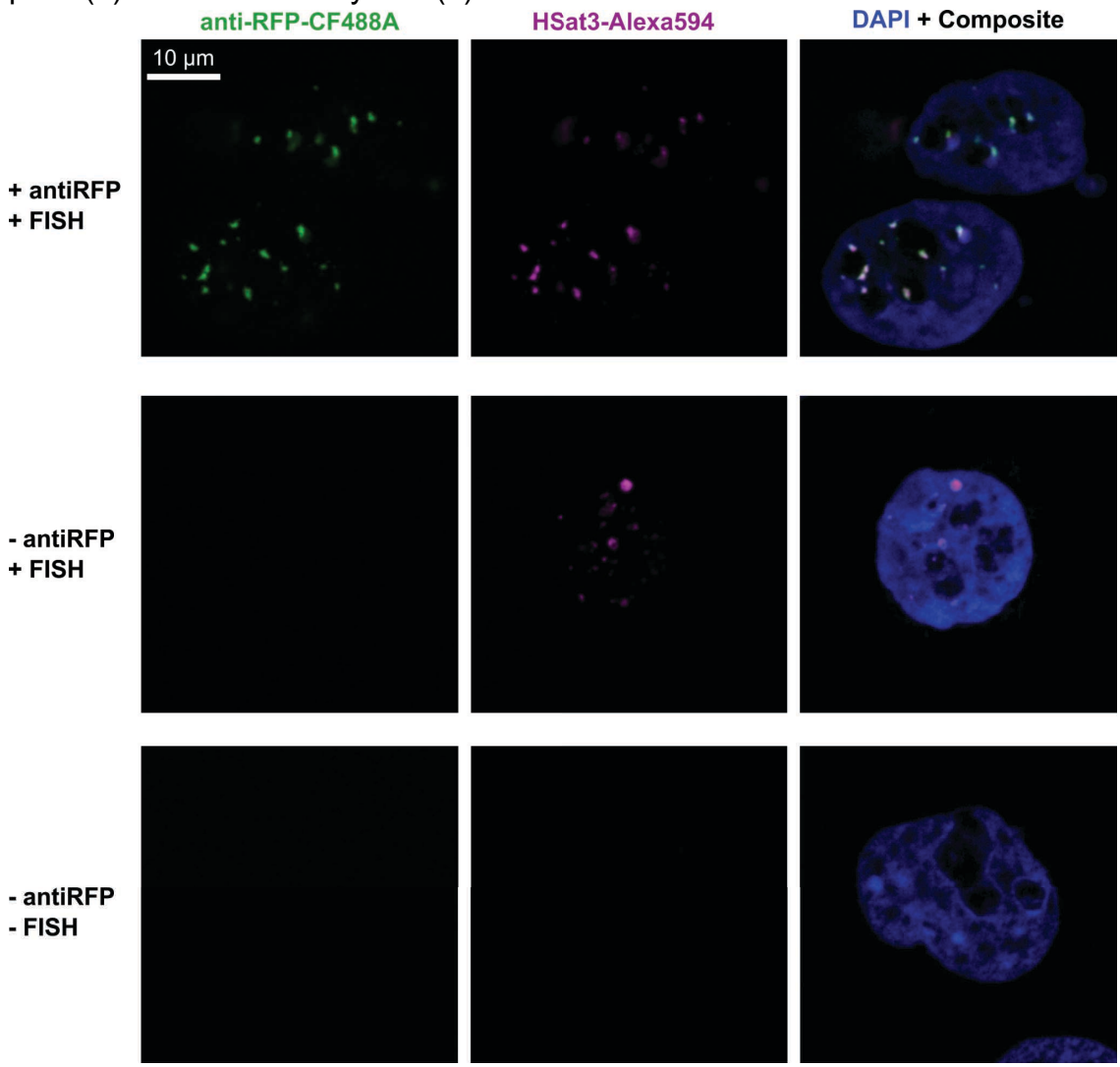

1371

1372 **Supplementary Figure 8:** JRK, TIGD3, and TEAD-family factors colocalize with HSat3.
1373 Negative and positive controls for imaging screens. Cells transfected with ZFsat3-mEGFP do
1374 not show strong bleedthrough into mScarlet channel. JRK and TIGD3 are previously reported
1375 HSat3 binding factors, both showing colocalization with ZFsat3-mEGFP.
1376

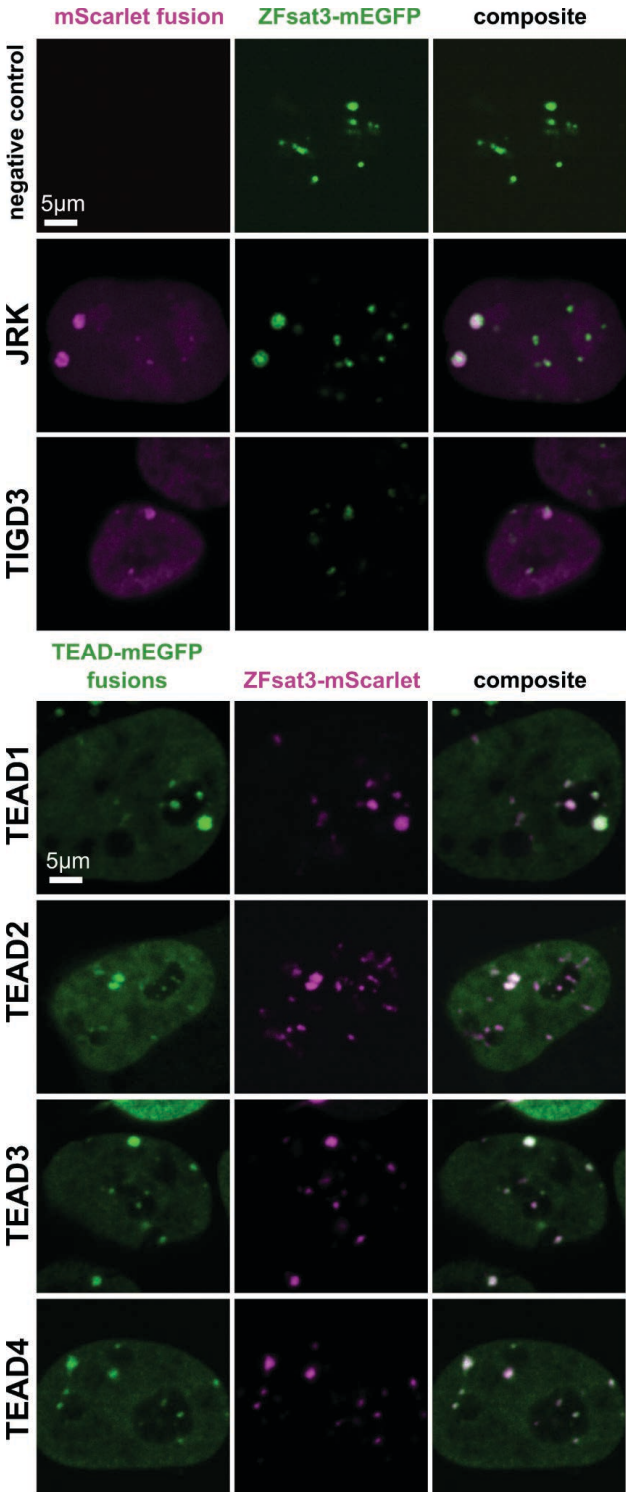

1377
1378 **Supplementary Figure 9:** (a) Ionomycin-stimulated NFAT-family factors colocalize to

1379 ZFsat3. (b) mScarlet-IRF3 is cytoplasmic in transfected 293T cells.

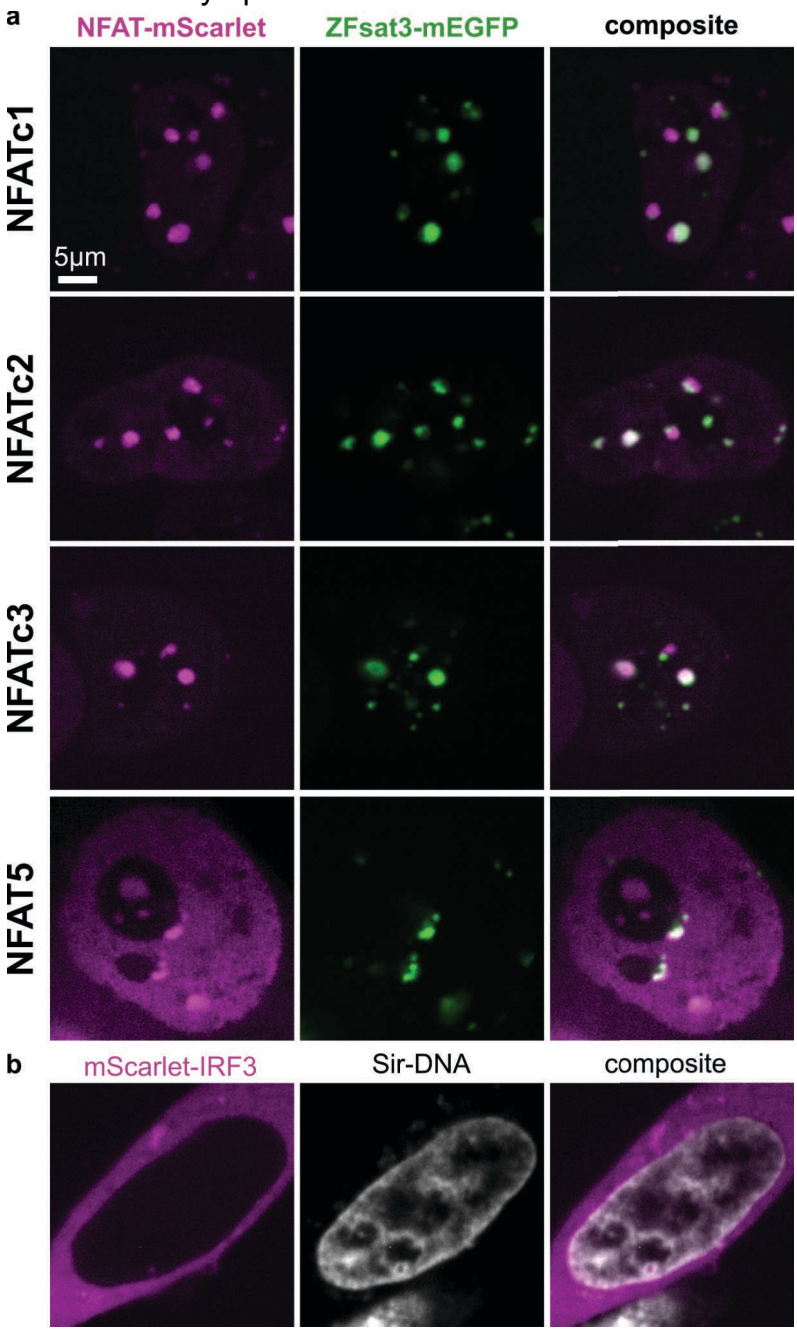

1380
1381
1382

Supplementary Figure 10: Subtle colocalization of SOX1 and NKX2-2 with ZFsat3-mEGFP. ROIs show a subset of foci are colocalized with HSat3.

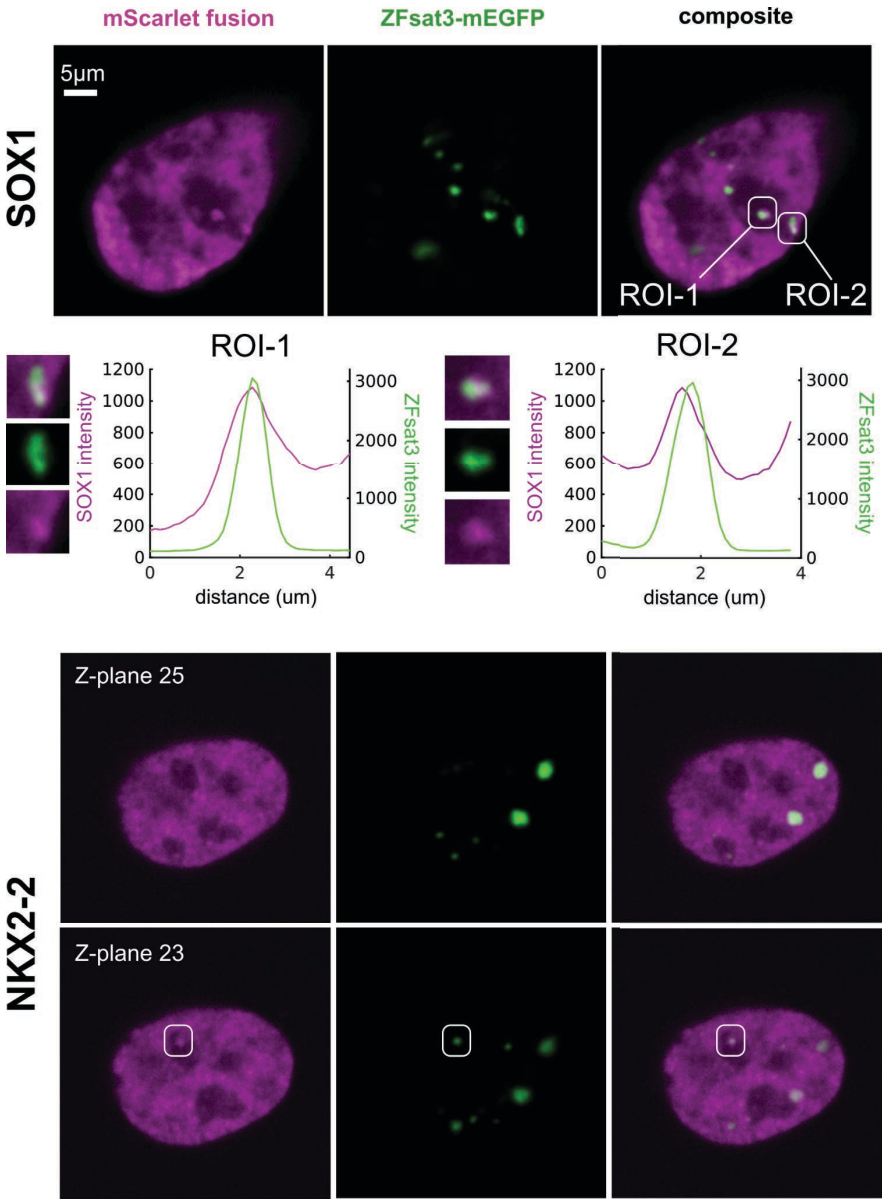

Supplementary Figure 11: Motifs for CUT Homeodomain containing factors. TF motif enrichment shows weak enrichment of motifs in HSat3 compared to TEAD4, however, imaging showed strong HSat3-binding (Figure 3b).

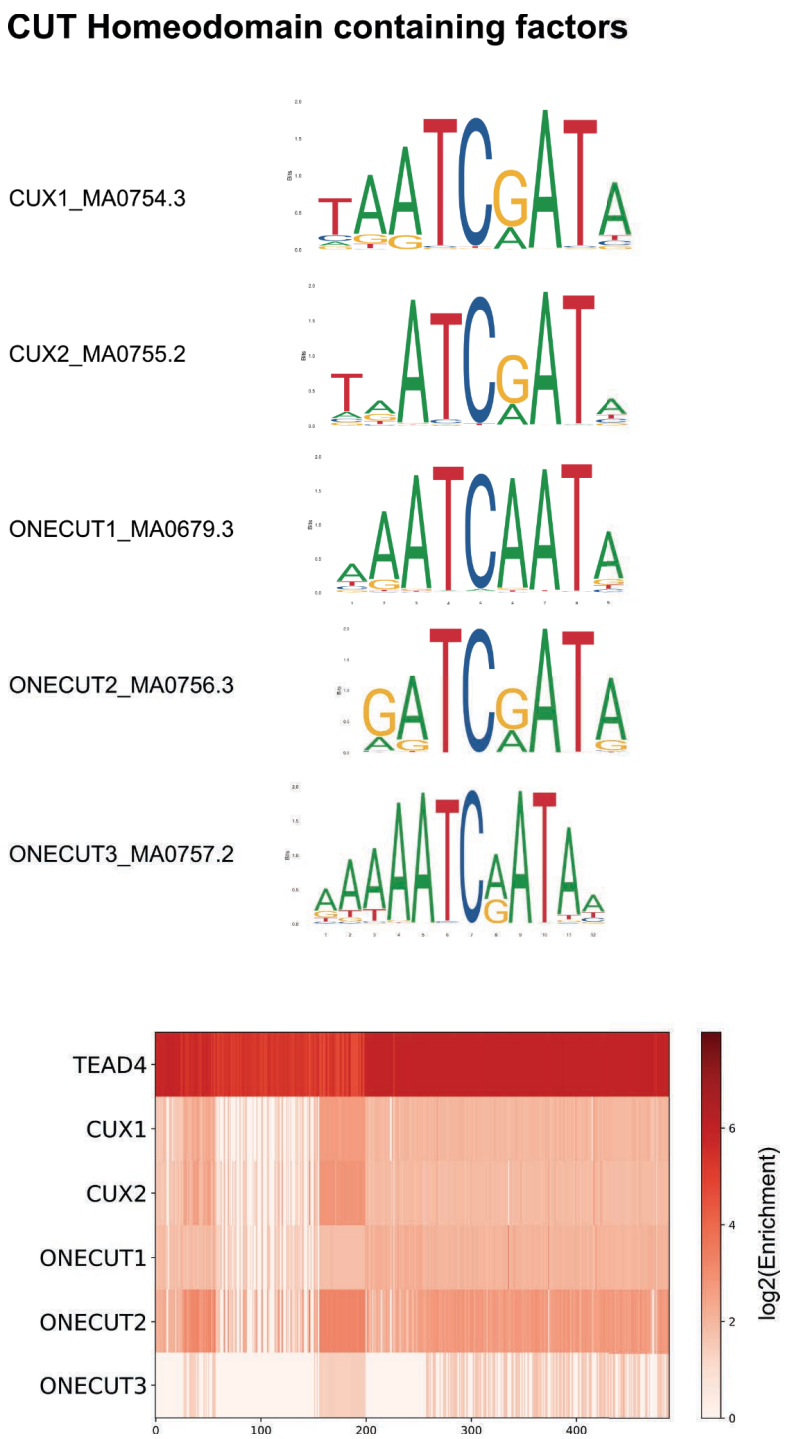

1394 **Supplementary Figure 12:** The PRDM15 ZF array binds HSat3. The nucleus is shown
1395 by increasing the display brightness.
1396

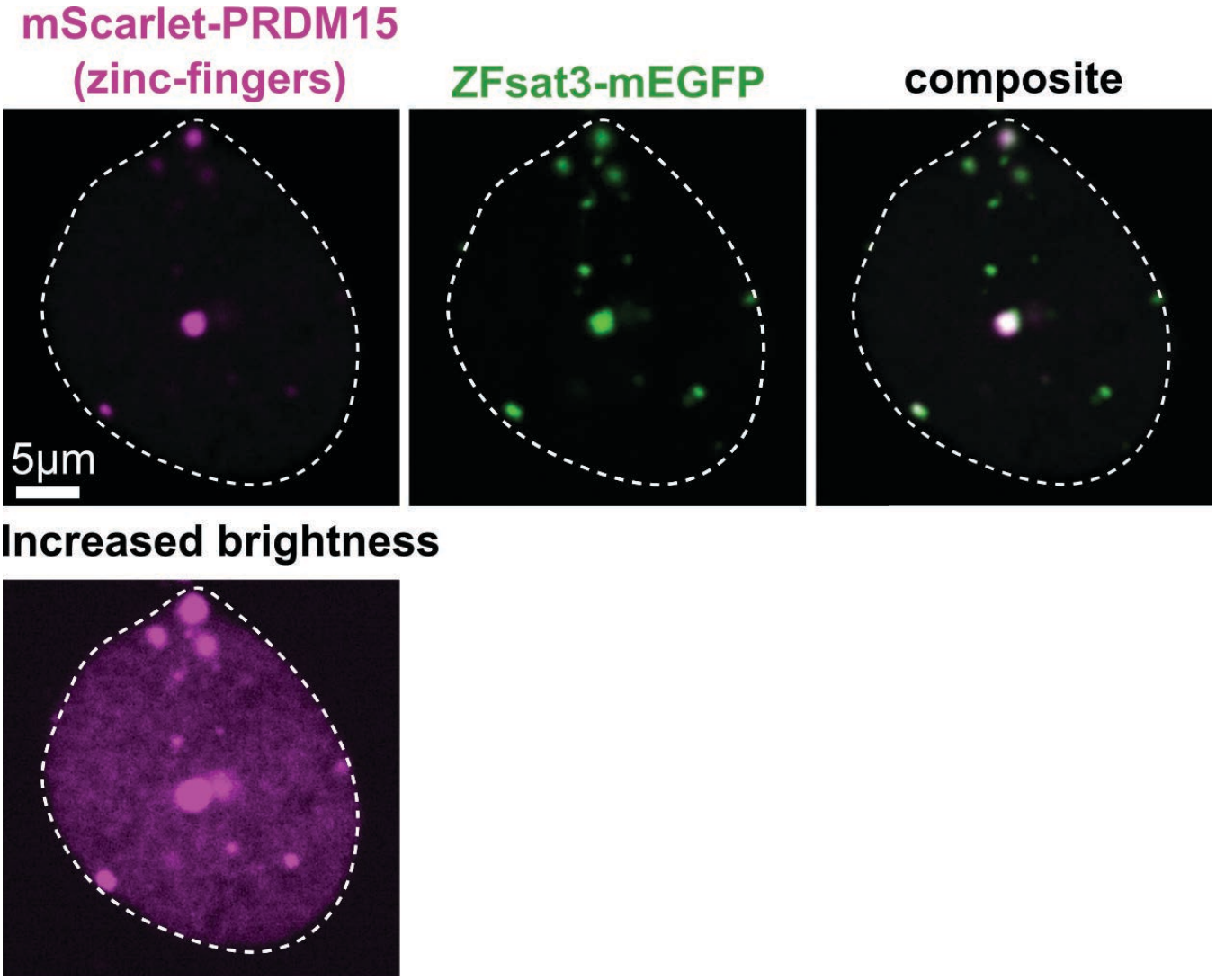

1397

1398 **Supplementary Figure 13:** Colocalization of ChIP-seq HSat3 candidates JUNB,
1399 HOXA7, HOXA9, HOXD9 with ZFsat3.

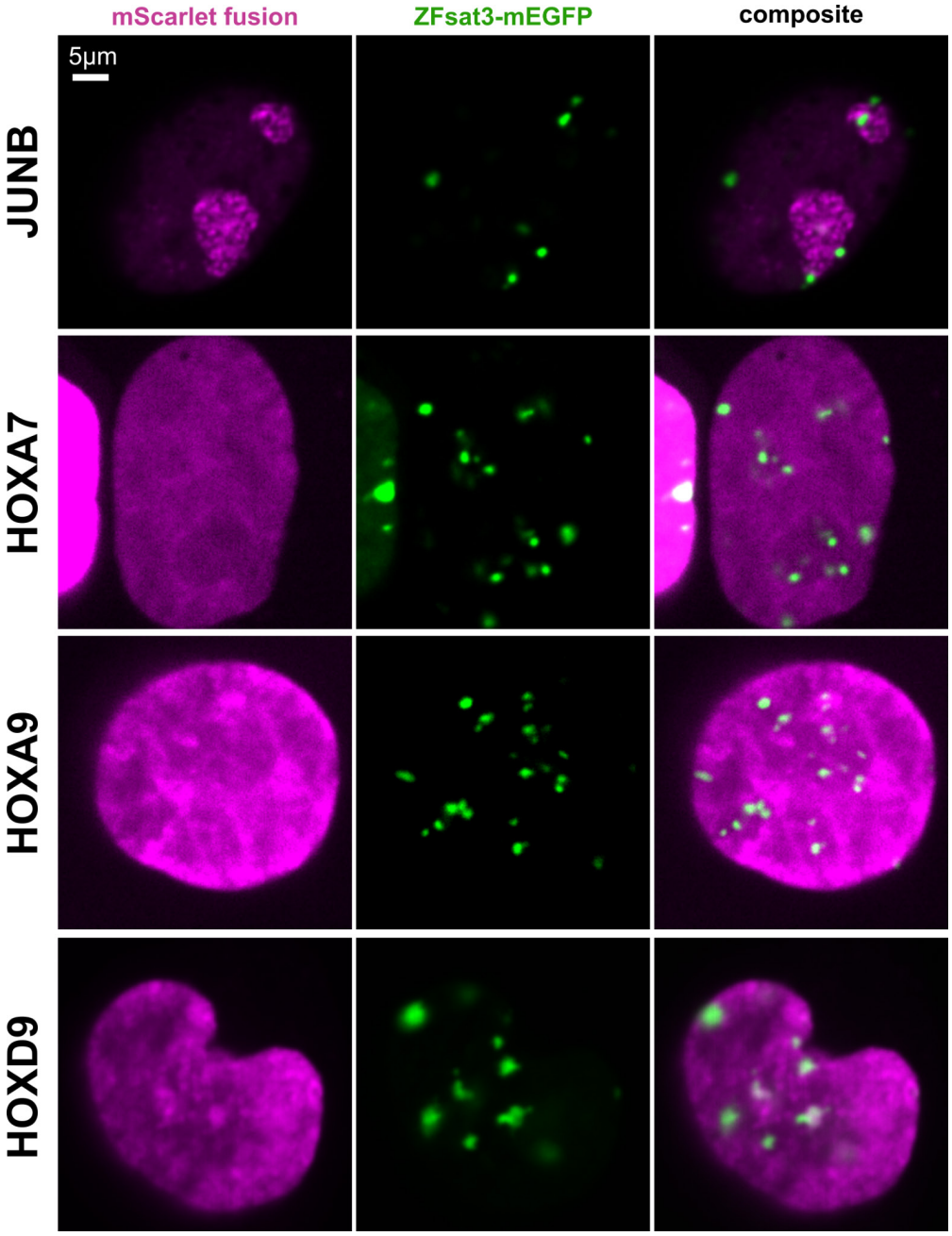

1400

1401 **Supplementary Figure 14:** A single z-plane of live-cell super-resolution (Airyscan)
1402 microscopy of endogenous YAP-eGFP in MCF10A cells. Arrows point to bright,
1403 nucleolar YAP foci.

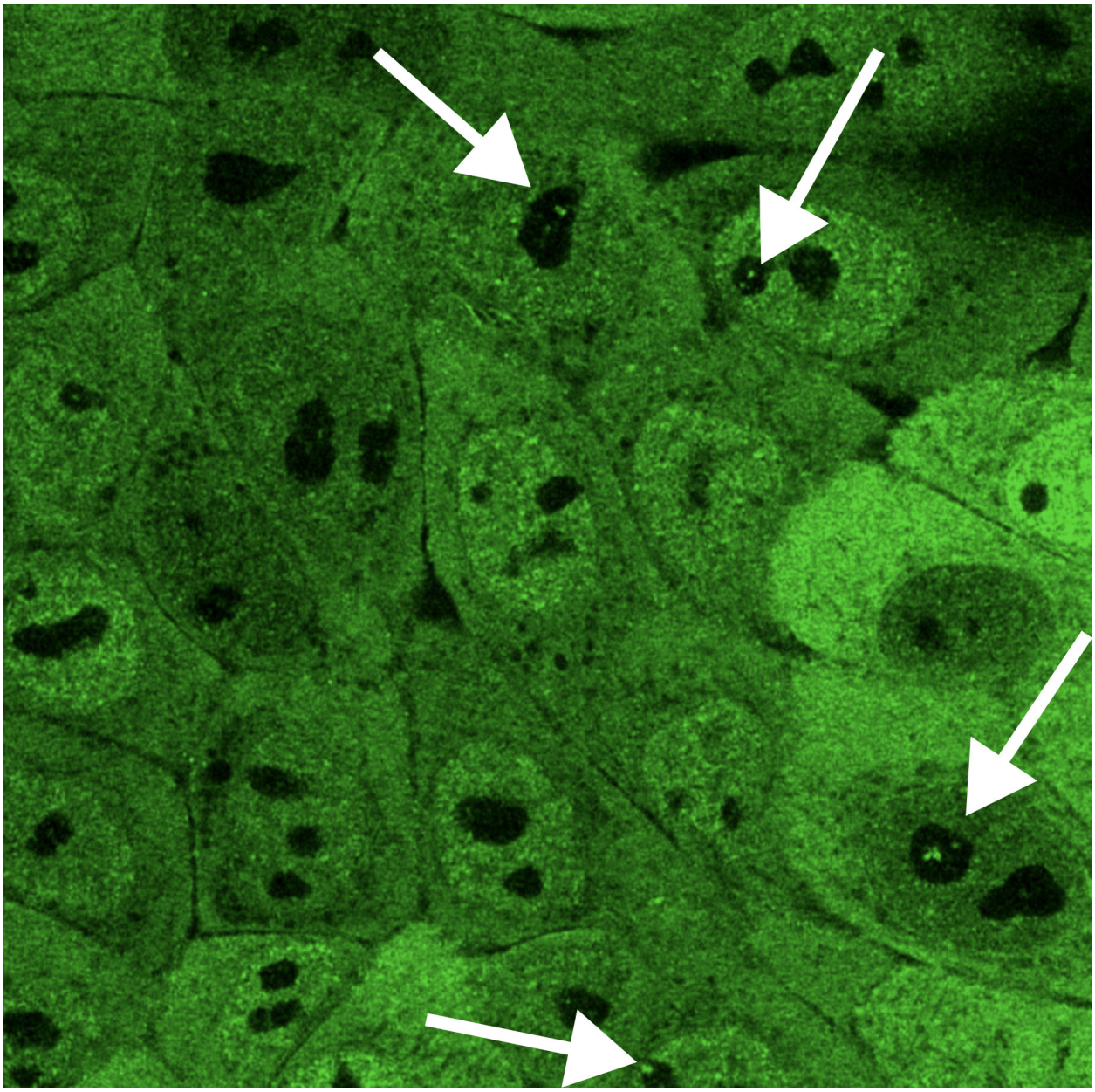

1404
1405

1406 **Supplementary Figure 15:** Colocalization of endogenous, nucleolar YAP-eGFP +
1407 TEAD1-HALO foci in H1 hESCs using Airyscan live-cell super-resolution imaging.

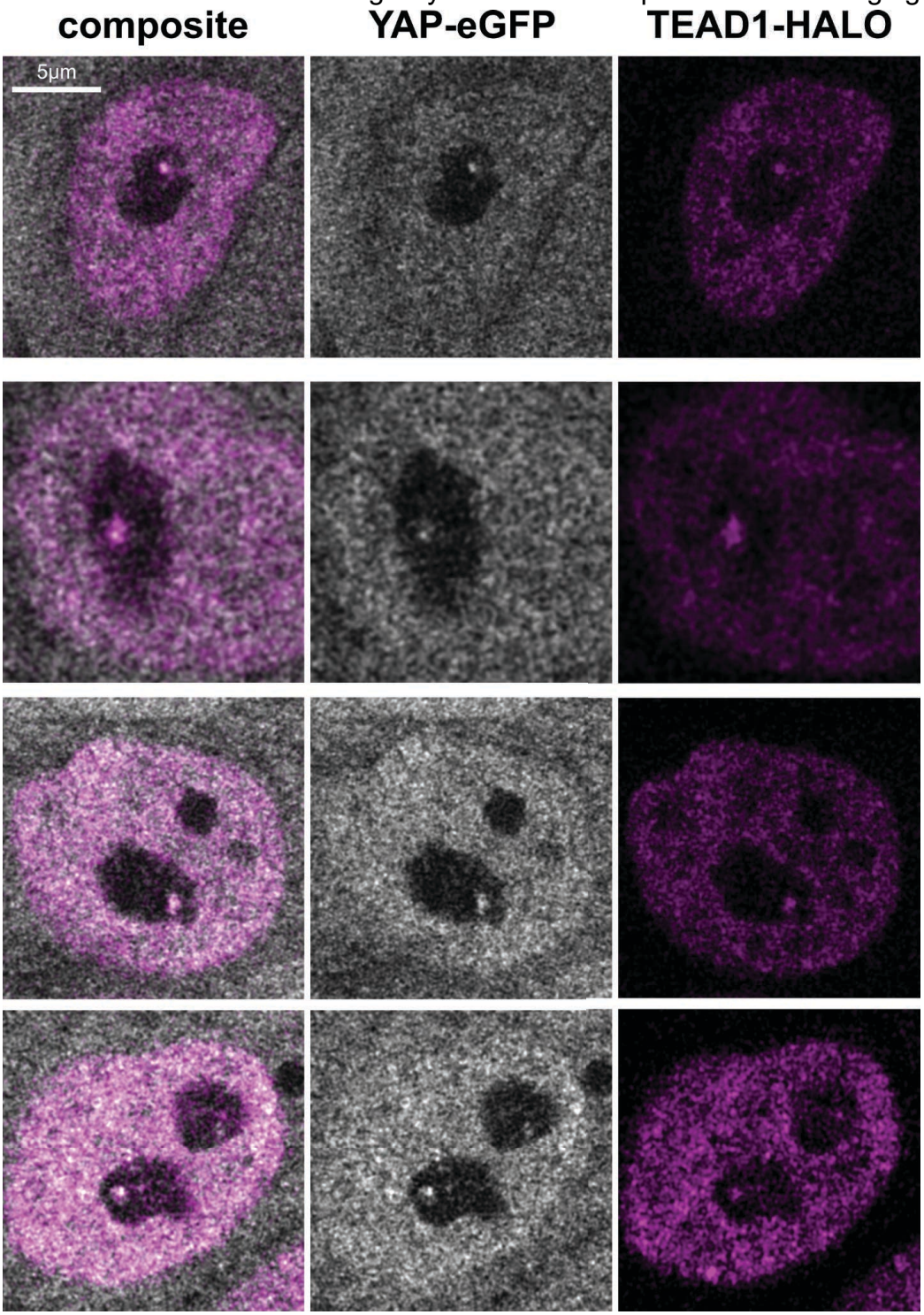

1408
1409

Supplementary Figure 16: Organization HSat3 and rDNA arrays across great apes. For each species, the chromosomes containing rDNA are depicted, with colored blocks for HSat3 and rDNA. Chromosome Y is included for all species. Chromosome 13 in Orangutans contains both HSat3 and rDNA. Whereas the human homolog, chromosome 9, only contains HSat3 (Figure 1a), suggesting the human ancestral state contained rDNA.

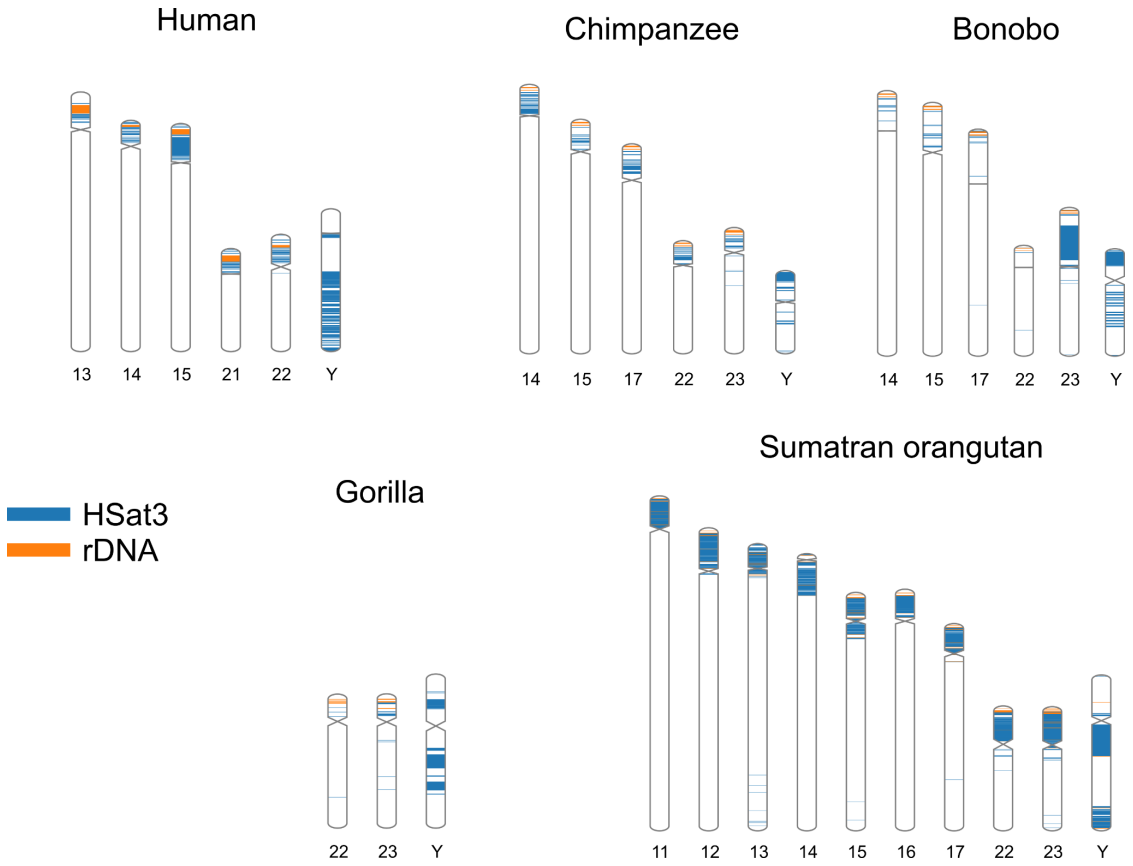

Supplementary Figure 17: rDNA-pol-I reporter assays are sensitive to actinomycin D at 50 ng/mL. Data points represent individual cells. The number of cells per condition are as follows: N(control DMSO)=314, N(control actD)=400, N(HSat3 DMSO)=314, N(HSat3 actD)=410. Data is from one biological replicate. Statistical significance was assessed using a one-tailed Wilcoxon rank sum test. Experiment was repeated twice with similar results.

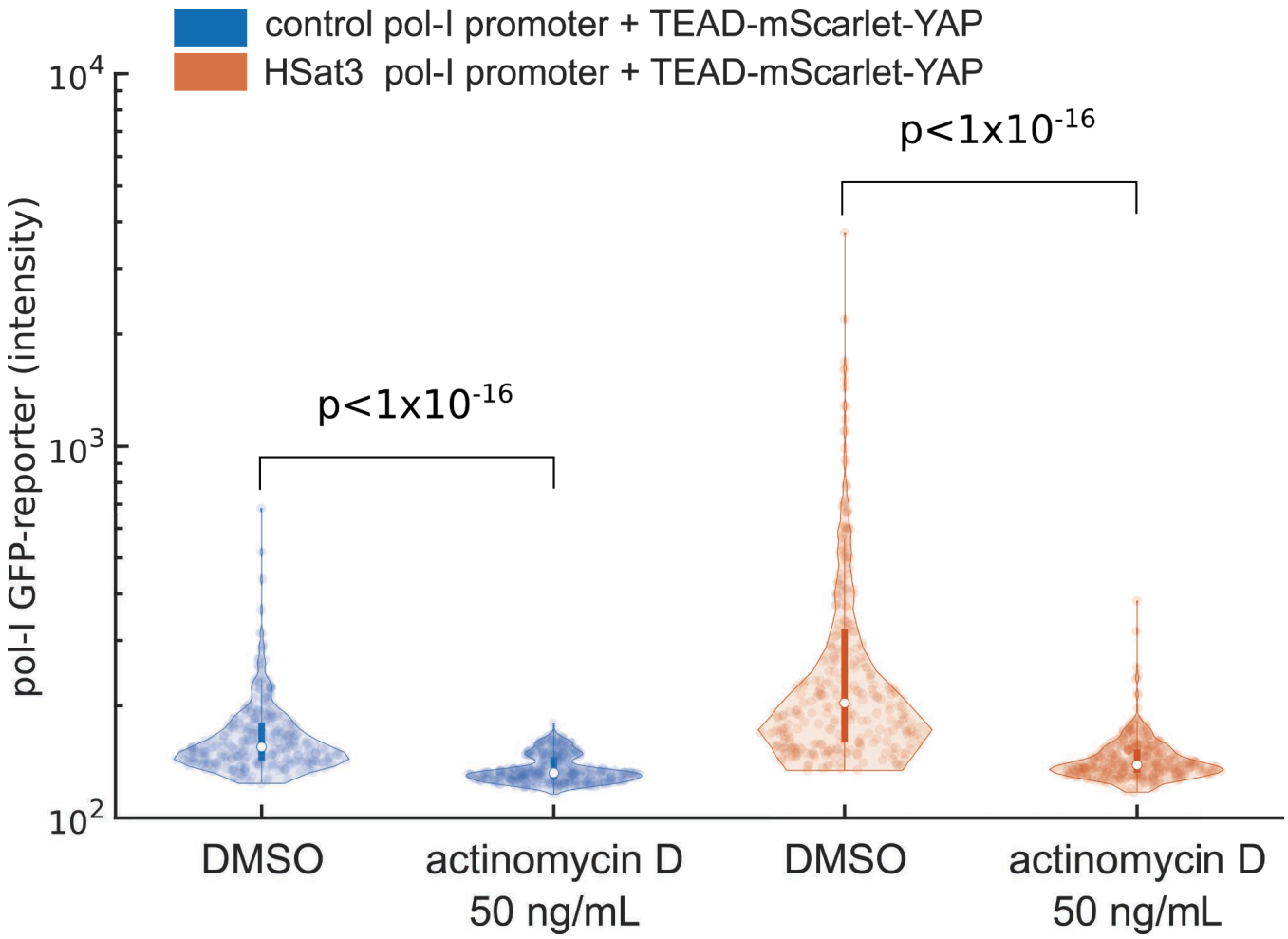

1437 **Supplementary Figure 18:** rRNA pol-I reporter assay is sensitive to Bmh21 at 2 μM.
1438 Data points represent individual cells. Following background correction due to
1439 autofluorescence of BMH21, 376 segmented cells remained with above zero signal
1440 intensity. We thus randomly selected 376 cells from the DMSO condition to compare
1441 reporter activity. Data is from one biological replicate. Statistical significance was
1442 assessed using a one-tailed Wilcoxon rank sum test. Experiment was repeated twice
1443 with similar results.

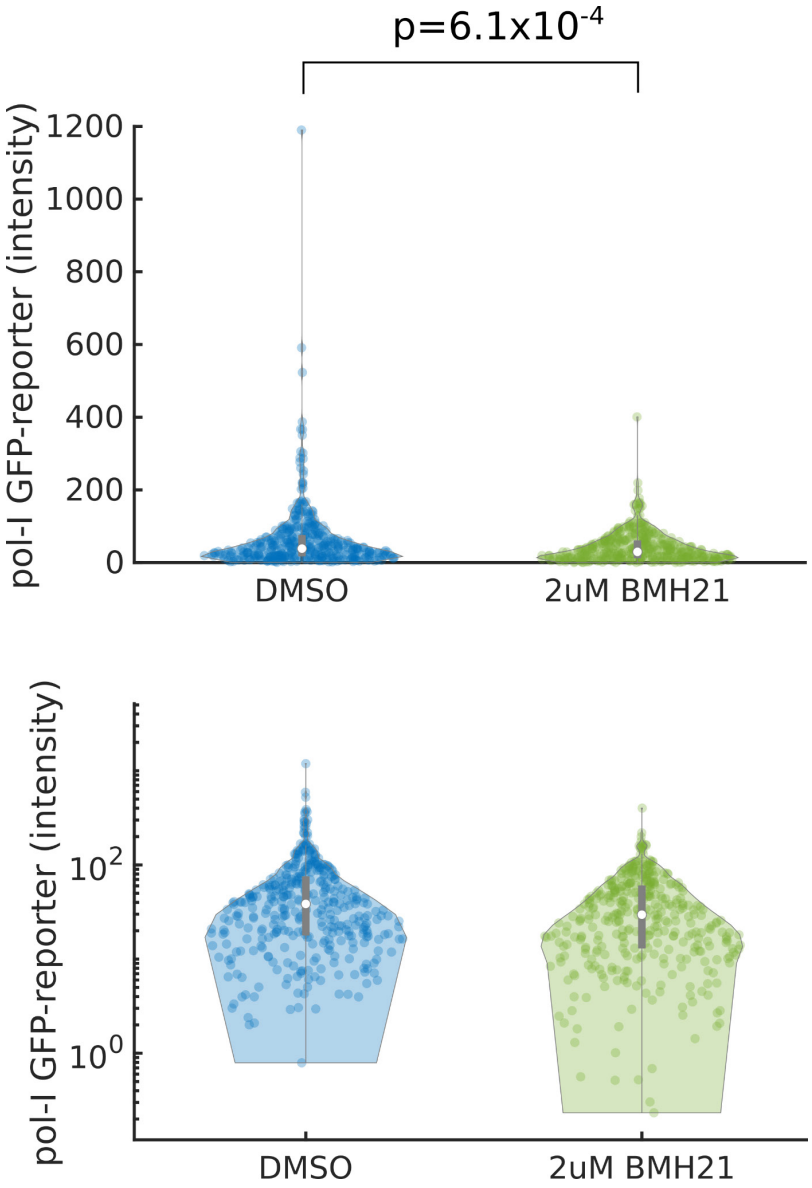

1444

1445 **Supplementary Figure 19:** Activity of HSat3-rDNA enhancer when co-transfected with
1446 2xNLS-mScarlet, TEAD1-YAP, and TEAD1-VP64. Data points represent individual
1447 cells. The number of cells per condition are as follows: N(NLS-mscarlet)=546,
1448 N(TEAD1-YAP)=556, N(TEAD1-VP64)=993. Data is from one biological replicate.
1449 Statistical significance was assessed using a one-tailed Wilcoxon rank sum test.
1450 Experiment was repeated twice with similar results.
1451

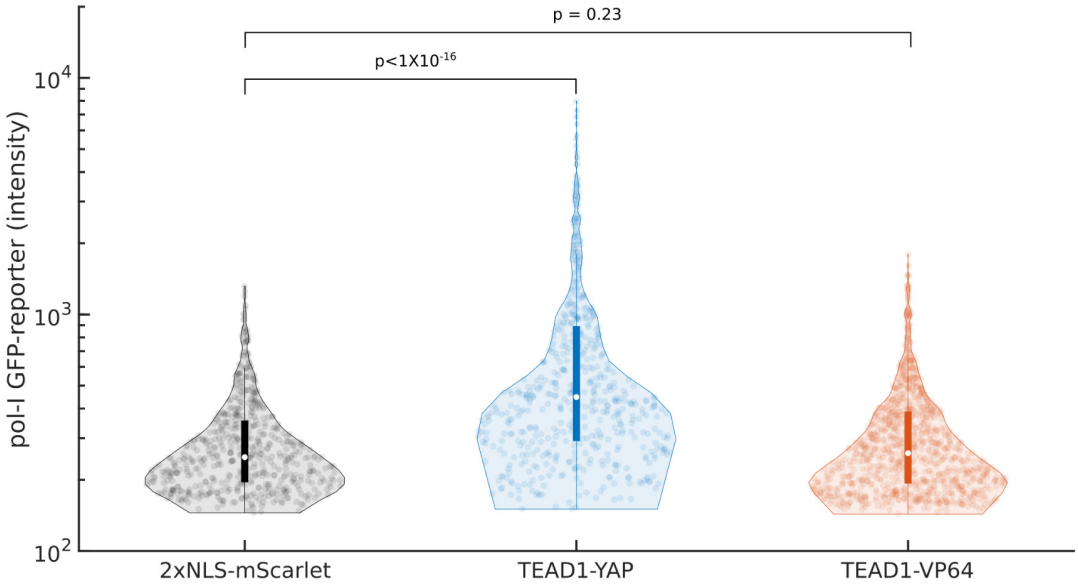

1452

Supplementary Figure 20: ZFsat3-mScarlet does not impact rRNA transcription in MCF10A cells. Expression of ZFsat3 only mildly increases EU signal, whereas ZFsat3-KM strongly represses EU signal (Figure 6d-e). Data points represent intensity values of segmented nucleoli. The number of nucleoli per condition are as follows: N(control mscarlet)=349, N(ZFsat3-mscarlet)=175. Data is from one biological replicate, repeated twice with similar results.

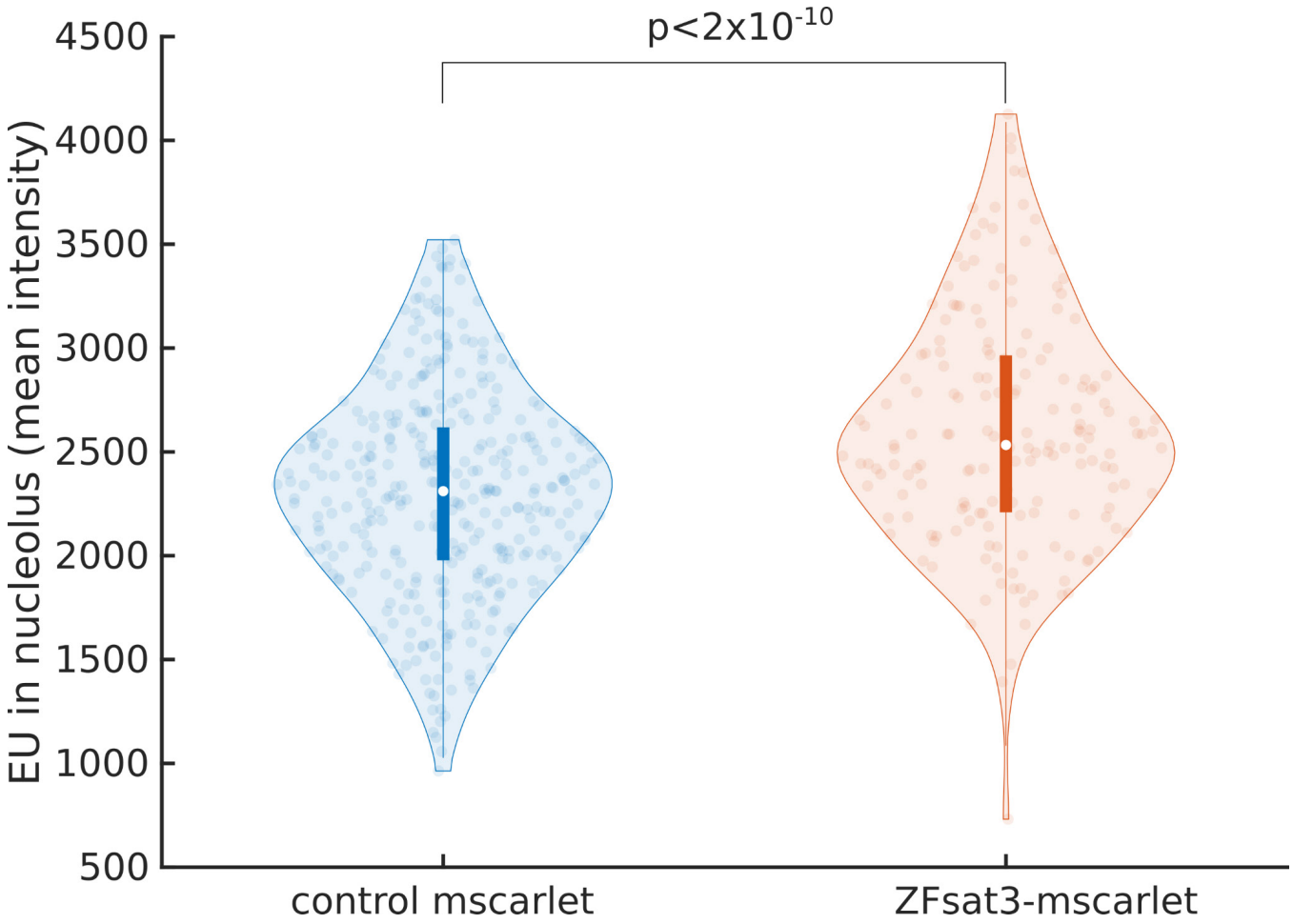

Supplementary Figure 21: Genomic PCR validation of YAP-degron clones in H1 hESC cells. Full length PCR amplicon for YAP-degron-p2a-puro is 3576 base pairs. Clones 2, 3, and 10 show a single band at the knock-in mark indicating homozygous knock-in.

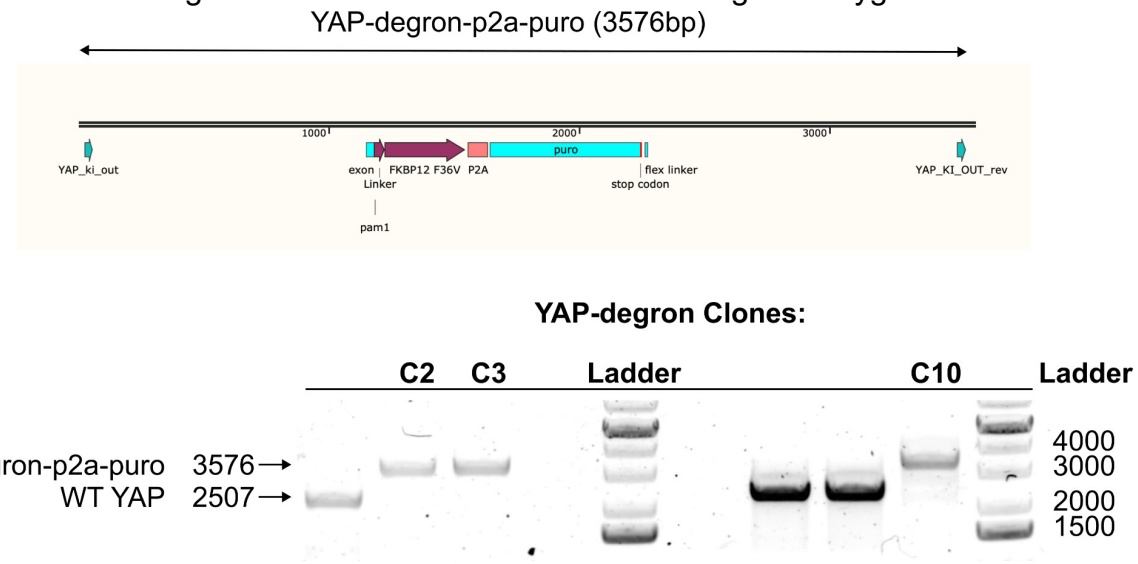

SUPPLEMENTARY DATA

[1] “motif_enrichments_HSat3.csv”: Data table of DNA binding motif enrichments for each HSat3 satellite element in the reference genome chm13v2.0 and 828 DNA-binding factors.

[2] “chip_seq_enrichments_HSat3.csv”: Data table of mean HSat3 enrichment from ChIP-seq datasets obtained from ENCODE and aligned to chm13v2.0.